

The local environment of the activator ions in the solid state lighting phosphor $\text{Y}_{3-x}\text{Ce}_x\text{Al}_5\text{O}_{12}$ [†]

Nathan George,^{‡,#} Géraldine Dantelle,[¶] Katharine Page,[§] Anna Llobet,[§] M.
Balasubramanian,^{||} Bradley F. Chmelka,^{*,‡} and Ram Seshadri^{*,[⊥],#}

Department of Chemical Engineering, University of California, Santa Barbara, CA, 93106, USA, Laboratoire de Physique de la Matière Condensée, École Polytechnique, UMR CNRS 7643, F-91128 Palaiseau, France, Los Alamos National Laboratory, Lujan Neutron Science Center, MS H805, Los Alamos, NM 87545, USA, X-ray Science Division, Advanced Photon Source, Argonne National Laboratory, Argonne, IL 60439, USA, and Materials Department and Materials Research Laboratory, University of California, Santa Barbara, CA, 93106, USA

E-mail: bradc@engineering.ucsb.edu; seshadri@mrl.ucsb.edu

Phone: (805) 893-6129. Fax: (805) 893-8797

[†]Electronic supplementary information (ESI) available: Further details. See DOI: xx.xxxx/xxxxxxxxxx

^{*}To whom correspondence should be addressed

[‡]Department of Chemical Engineering, University of California, Santa Barbara, CA, 93106, USA

[¶]Laboratoire de Physique de la Matière Condensée, École Polytechnique, UMR CNRS 7643, F-91128 Palaiseau, France

[§]Los Alamos National Laboratory, Lujan Neutron Science Center, MS H805, Los Alamos, NM 87545, USA

^{||}X-ray Science Division, Advanced Photon Source, Argonne National Laboratory, Argonne, IL 60439, USA

[⊥]Materials Department and Materials Research Laboratory, University of California, Santa Barbara, CA, 93106, USA

[#]Mitsubishi Chemical Center for Advanced Materials, University of California, Santa Barbara, CA, 93106, USA

Abstract

Solid-state lighting, typically employing a blue light-emitting diode in conjunction with a yellow phosphor that partially down-converts the blue radiation, is an efficient way of creating white light. Cerium-doped yttrium aluminum garnet $Y_{3-x}Ce_xAl_5O_{12}$ (abbreviated YAG:Ce) is perhaps the best-known phosphor used for this purpose. Despite its widespread use, key details of the environment of the Ce^{3+} activator ions in YAG:Ce remain somewhat unclear, associated with the difficulties in probing the very small Ce^{3+} substitution amounts, approaching a few %. We present here, a detailed study of this unique and very useful material using a combination of synchrotron X-ray and neutron scattering, neutron total scattering, EXAFS, ^{27}Al and ^{89}Y NMR, and EPR measurements, in order to construct a consistent picture of the local structure around Ce^{3+} in the YAG lattice. The different techniques confirm that the Ce is stoichiometrically incorporated into the structure as Ce^{3+} , which is randomly distributed. Total neutron scattering in conjunction with reverse Monte-Carlo modeling allows the environment of Ce to be probed independently of the environment of the Y site that it substitutes. These complement Ce K-edge EXAFS measurements, which reveal highly compressed Ce–O polyhedra, with effective bond valence sums close to 3.3 ± 0.1 . There is a small expansion of the average Ce–O distances compared to the average structure Y–O distances of about 3%, which relaxes to the average distance by the 5th coordination shell around Ce. Both neutron scattering and EXAFS suggest, from the Debye-Waller factors, a rigid environment around Ce^{3+} , which we propose is related to the high emission efficiency and robust thermal performance of YAG:Ce, since not all phonon modes are available for non-radiative transitions at LED operating temperatures. ^{27}Al and ^{89}Y magic-angle spinning NMR measurements make use of the paramagnetic spin on Ce^{3+} to particularly probe the effects of Ce^{3+} substitution in YAG. Electron paramagnetic resonance (EPR) measurements of the Ce^{3+} unpaired spin at 4 K yield further details of the structure. Taken together, the studies presented here emphasize the complementary ability of scattering and spectroscopy to probe, in exquisite detail, structural intricacies in functional materials and how they relate to property.

INTRODUCTION

Solid-state lighting consisting of a blue, semiconducting InGaN source in conjunction with partial blue-to-yellow down-conversion, enabled by an appropriate phosphor, provides a promising new approach to efficient, general purpose lighting. Advantages of such light sources include their long-life, durability, color-stability, and their relatively benign environmental footprint, *eg.*, they are mercury-free.^{1,2} The most frequently used solid state lighting devices employ as a phosphor cerium-doped yttrium-aluminum garnet ($\text{Y}_{3-x}\text{Ce}_x\text{Al}_5\text{O}_{12}$, YAG:Ce) suitably incorporated on a blue InGaN light-emitting diode.³⁻⁶

Cerium-doped YAG was in fact first described by Blasse and Brill in 1967, for use in displays.⁷ When bright-blue InGaN sources first became available,⁸ YAG:Ce was determined to be close to ideal for the generation of white light *via* partial down-conversion, due to its favorable optical characteristics, which include appropriate matching of its excitation spectrum to blue InGaN sources, high efficiency, and an emission spectrum in the complementary (to blue) color region. The absorption peaking around 460 nm and emission peaking around 540 nm are known to occur from the transition of Ce^{3+} between the Ce $[\text{Xe}]4f^15d^06s^0$ ($^2F_{5/2}$, $^2F_{7/2}$) and $[\text{Xe}]4f^05d^16s^0$ ($^2D_{3/2}$, $^2D_{5/2}$) states.⁹ The energy gap between these two states is significantly increased from what it would be for the isolated ion by crystal field splitting of Ce^{3+} 5d states when the Ce^{3+} ion replaces the smaller Y^{3+} ion in the YAG structure.¹⁰ YAG:Ce is known to be extremely bright, with quantum efficiencies at room temperature exceeding 85%.¹¹ Although the reason for the blue absorption and yellow emission is well known, the crystal-chemical reasons for such high quantum efficiency in YAG:Ce are yet to be elucidated, as are reasons for the thermal robustness of the luminescence.¹²

The optical properties of YAG:Ce, including temperature-dependent phenomena, have been well studied. For example, zero-phonon lines from low-temperature spectroscopy were correlated with lattice phonon energies, and characteristics of the crystal-field splitting of the 4f and 5d states of Ce in YAG were determined from the same low-temperature

spectroscopy.¹³ Temperature effects on the luminescence of YAG:Ce were also determined; at temperatures above 100 °C (especially for higher Ce concentrations) lower efficiency due to thermal quenching amounts to around a 5% loss in quantum efficiency.¹² As temperature and/or Ce concentration is increased, the rate of efficiency loss becomes more dramatic. Effects of Ce concentration on the optical properties of YAG:Ce were first studied by Tien et al., who found red-shifts in the excitation and emission maxima with increasing Ce concentration.¹⁴ Shortly thereafter, a kinetic model was used to describe the concentration-dependent efficiency of YAG:Ce,¹⁵ and more recently, Setlur and Srivastava further examined the relationship between optical characteristics in YAG:Ce, finding that lower-energy Ce³⁺ sites may be present in YAG:Ce with relatively high Ce concentrations (around $x = 0.09$ in $Y_{3-x}Ce_xAl_5O_{12}$).¹⁶ The lower-energy Ce sites lead to a red-shift in emission, and were attributed to either Ce-Ce pairs and/or Ce in perturbed lattice sites.

Some studies have also examined structure-property relationships in luminescent garnets, such as one study that correlated emission and excitation wavelength to the average structure of the active site in garnets.¹⁷ Furman et al. studied the local structure of YAG:Ce nanoparticles using synchrotron total X-ray scattering,¹⁸ and Pan *et al.* used Cu- $k\alpha$ X-ray diffraction to correlate the red shift of Gd³⁺-substituted YAG:Ce nanoparticles with their structure.¹⁹ In one first-principles study on the local structure of Ce in YAG, the results from calculations predicted an expansion of 3% of the nearest 4 Ce–O bonds, but only a 0.03% expansion of the next-nearest 4 Ce–O bonds, when compared to the undoped material.²⁰ Another ab-initio study examined the local structure of Ce³⁺ in YAG, and found that the local Ce–O distances expand by about 1% to 2% in $Y_{2.875}Ce_{0.125}Al_5O_{12}$.²¹ This study also found that the expansion around Ce is observable and decreases in magnitude out to the 5th coordination shell. A recent study looked at the local structure of the Ce³⁺ ion using Ce K-edge EXAFS, and found that the nearest 8 Ce–O distances are slightly larger than the Y–O distances in YAG:Ce by about 3% in $Y_{2.97}Ce_{0.03}Al_5O_{12}$, but did not see any significant expansion of the lattice past the first three coordination shells around Ce.²²

In light of the great importance of this material, and the challenges associated with the careful structural analysis of small substituents in crystalline materials, we have employed a suite of powerful state-of-the-art structural probes, focusing on the local structure of the Ce ion and its interaction with the YAG host structure. The scattering and spectroscopic techniques used here yield powerful insights regarding the optical properties of YAG:Ce. More generally, these techniques enable precise structural analysis of a dopant ion at a very small concentration (around 1 mole %). Such analysis is useful not only when investigating phosphors, but also when investigating other important materials with small doping amounts, such as heterogeneous catalysts, semiconductors, thermoelectrics, and luminescence up-conversion materials. With recent advances in synchrotron X-ray²³ and neutron powder diffraction²⁴ techniques, structural information from inorganic materials can be garnered with unprecedented accuracy. Recently developed Monte Carlo simulation techniques enable detailed statistical investigation of total neutron scattering data,²⁵⁻²⁷ which to date has not been used on phosphor materials. X-ray absorption near edge structure (XANES) and extended X-ray absorption fine structure (EXAFS) yield crucial complementary information about the oxidation state and local structural environments of the Ce³⁺ ions. High-resolution magic-angle spinning solid state nuclear magnetic resonance (NMR) provides complementary structural information to scattering measurements on the local electronic and spin environment, as does electron paramagnetic resonance (EPR). In particular, we demonstrate the usefulness of the paramagnetism of Ce³⁺ as an internal contrast reagent in the NMR studies. This broad range of techniques enables a new understanding of the local structure of Ce in YAG, and not only sheds new light on a well-known material, but also is expected to enhance the rational design of new phosphor materials.

MATERIALS AND METHODS

Preparation of samples. Samples of $Y_{3-x}Ce_xAl_5O_{12}$ with $x = 0, 0.02, 0.04, 0.06, 0.08,$ and 0.09 were prepared using conventional solid-state preparation methods.^{28,29} Starting materials consisting of stoichiometric amounts of Y_2O_3 (Sigma-Aldrich, 99.9%), Al_2O_3 (Sumitomo AKP-50, >99.99%), and CeO_2 (Cerac, 99.9%), with 5% by mass BaF_2 (Sigma-Aldrich, 99.9%), and 0.5% by mass NH_4F (Sigma-Aldrich, 99.99%) as sintering agents (flux), were ground in an agate mortar and pestle, placed in alumina crucibles, and fired at $1500^\circ C$ for 5 hours in an alumina tube furnace under 0.2 l/min 5% H_2/N_2 gas flow. The amounts of flux and Ce were optimized by the emission intensity, resulting in optimum values of 5 mass % BaF_2 , 0.5 mass % NH_4F , and a Ce concentration of $x = 0.06$ ($Y_{2.94}Ce_{0.06}Al_5O_{12}$). The measured quantum efficiency of the optimized sample was 87%. Samples for XANES/EXAFS and total neutron scattering ($Y_{2.91}Ce_{0.09}Al_5O_{12}$) were prepared with stoichiometric amounts of Y_2O_3 (Sigma-Aldrich, 99.9%), Al_2O_3 (Sumitomo, 99.9%), and CeO_2 (Cerac, 99.9%), which was ground in an agate mortar and pestle, pressed into pellets, placed in alumina crucibles on a bed of sacrificial powder, and fired at $1600^\circ C$ for 96 hours in an alumina tube furnace under 0.2 l/min 5% H_2/N_2 gas flow. After the starting materials had been reacted, the phosphor cakes were ground into fine powders.

Synchrotron X-ray and neutron scattering. High-resolution synchrotron powder diffraction data were collected using the 11-BM beamline at the Advanced Photon Source (APS) at Argonne National Laboratory, using an average wavelength of $\lambda = 0.412154 \text{ \AA}$. Other details regarding the experimental setup can be found elsewhere.²³

Neutron powder diffraction was performed on the HIPD and NPDF instruments at the Los Alamos Neutron Science Center at Los Alamos National Laboratory. Powder samples were placed in vanadium cans, and time-of-flight neutron data was collected at 295 K on the HIPD instrument from 8 detector banks at $\pm 14^\circ, \pm 40^\circ, \pm 90^\circ$ and $\pm 153^\circ 2\theta$. For the NPDF measurements, powder samples were placed in vanadium cans, and time-of-flight

neutron data were collected at 15 K and 295 K from 4 detector banks at 14° , 40° , 90° and $153^\circ 2\theta$.

Crystal structures were refined using the programs XND³⁰ and the EXPGUI front end for the refinement program General Structure Analysis System (GSAS).³¹ Simultaneous refinements to the X-ray and neutron scattering data were completed by adjusting the profile shapes and unit cells during the LeBail fits, refining neutron absorption coefficients, instrument parameters, and the backgrounds (10-term Chebyshev polynomial function), then refining the atomic positions, and finally the atomic displacement parameters and Y/Ce occupancies. When completed, all available structural parameters were allowed to refine simultaneously. Crystal structures were visualized using the software VESTA.³²

Neutron total scattering and Reverse Monte Carlo (RMC) simulations. Time-of-flight (TOF) total neutron scattering on $\text{Y}_{2.91}\text{Ce}_{0.09}\text{Al}_5\text{O}_{12}$ was carried out at 295 K on the NPDF instrument at the Los Alamos Neutron Science Center at Los Alamos National Laboratory. The data were extracted using PDFGETN,³³ with $Q_{max} = 31 \text{ \AA}^{-1}$. The uncertainty from the PDF measurement is around 0.1 \AA ($\Delta r = \pi/Q_{max}$).³⁴ PDFGUI was used to fit a symmetric model to the PDF out to 50 \AA .³⁵ Reverse Monte Carlo simulations were run using RMCPROFILE version 6 and a $4 \times 4 \times 4$ unit cell with 10240 atoms.^{36,37} These simulations were simultaneously constrained by the $S(Q)$ Bragg profile and the $G(r)$. All atom–atom distances were subject to a hard-sphere cutoff at 1.576 \AA . Ce and Y atoms were allowed to exchange positions with a 5% chance of each move being an atom swap. Eight runs were averaged for better statistics, and simulations were run for a total of approximately 915 moves per atom.

X-ray absorption near edge structure (XANES) and extended X-ray absorption fine structure (EXAFS) measurements. Ce K-edge X-ray absorption (XAS) studies were carried out at sector 20-ID beamline at the Advanced Photon source at 295 K.³⁸ The fifth harmonic of the undulator was used along with full scanning of the undulator. The inci-

dent beam was monochromatized using a pair of Si (311) crystals. Higher order harmonics were suppressed by detuning the monochromator to reduce the incident X-ray intensity by $\sim 15\%$. Argon-filled ion chambers were used for the Io, It, and Iref detectors. A cold pressed pellet of CeO₂ in BN was placed between It and Iref to provide internal calibration for the alignment of edge position. The Ce K-edge of the Ce in the $x = 0.09$ YAG:Ce sample was measured on a pure pellet of the sample in fluorescence geometry using a 13-element energy dispersive germanium detector, operated at a total count rate of ~ 80 KHz per element. The Y background fluorescence signal impinging the Ge detector was selectively reduced by using several layers of thin aluminum foil, and care was taken to account for dead-time associated with saturation of the detector.

The CeO₂ absorption edge was calibrated to 40.473 keV as previously measured.³⁹ Simulations of the data were performed using the ARTEMIS code,⁴⁰ with fits performed in the k^2 regime; fits in other k^x regimes gave results in good agreement with the k^2 regime. The k -space range was 2.77 \AA^{-1} to 16 \AA^{-1} , giving a spacial resolution of about 0.1 \AA . Ten variables were used with an estimated 25 independent points.

Solid-state ²⁷Al and ⁸⁹Y Nuclear Magnetic Resonance (NMR) spectroscopy. Solid-state ²⁷Al and ⁸⁹Y magic-angle spinning (MAS) NMR spectroscopy was used to investigate the local structure of YAG:Ce. The single-pulse and T_1 -filtered ²⁷Al NMR experiments were performed at 295 K on a Bruker AVANCE IPSO NMR spectrometer, with an 18.8 T narrow-bore superconducting magnet, operating at a frequency of 208.52 MHz for ²⁷Al nuclei, which are 100% naturally abundant. A Bruker 3.2 mm H-X-Y triple-resonance MAS probe head was used with zirconia rotors and Kel-F® caps, with a MAS rate of 24 kHz. Radio frequency (RF) pulse lengths and power levels were calibrated to achieve a 15° rotation ($\pi/12$) of the net ²⁷Al magnetization ($2.7 \mu\text{s}$) to ensure quantitative measurements,⁴¹ and were calibrated with respect to the longitudinal spin-lattice relaxation time (T_1) to ensure the spectra were fully quantitative (recycle delay of 40 s). An external AlN sample was

used as a spin-counting standard, which confirmed 100 % visibility of all ^{27}Al nuclei in all samples. Chemical shifts were referenced to 1 M $\text{Al}(\text{NO}_3)_3$ at 0 ppm.

^{27}Al spin-lattice relaxation-time behaviors of the YAG:Ce samples were established by using complementary 1D saturation-recovery and T_1 -filtered ^{27}Al MAS NMR spectra. 1D saturation-recovery ^{27}Al MAS NMR spectra were acquired for a range of times, τ , between 0.05 s and 70 s on a Bruker AVANCE IPSO NMR spectrometer, with an 11.7 T wide-bore superconducting magnet, operating at a frequency of 130.28 MHz for ^{27}Al nuclei. A Bruker 4 mm H-X-Y triple-resonance MAS probe head was used with zirconia rotors and Kel-F® caps, with a MAS rate of 14 kHz. A RF pulse length of $2.51 \mu\text{s}$ was calibrated with the power level for a 90° rotation of the net magnetization of octahedral ^{27}Al nuclei, and a 400-pulse saturation train with $2 \mu\text{s}$ between saturation pulses with a 0.1 s recycle delay was used. The long saturation train was not rotor-synchronized, leading to a saturation of the central and satellite transitions, minimizing effects from population transfer between $\pm 5/2$ and $\pm 3/2$ to $\pm 1/2$ Zeeman levels.^{42,43} 1D T_1 -filtered ^{27}Al MAS NMR spectra (on the 18.8 T NMR spectrometer) were acquired with two consecutive ^{27}Al 90° pulses, followed by a time delay, $t_{T_1} = 15$ s, and then another ^{27}Al 90° pulse before detection to suppress octahedral ^{27}Al signals from species with spin-lattice relaxation times shorter than the respective $t_{T_1} = 15$ values. The 1D T_1 -filtered ^{27}Al MAS NMR spectra were scaled using an appropriate constant $c > 1$ to account for decreased signal intensity due to T_1 relaxation effects, which allows for remaining signals to be normalized for comparison with the single-pulse ^{27}Al spectra.

The ^{89}Y NMR experiments were performed at the National High Magnetic Field Laboratory in Tallahassee, Florida, on a narrow-bore Magnex 19.6 T magnet fitted with a Bruker console, operating at a frequency of 40.804 MHz for ^{89}Y nuclei, which are 100% naturally abundant. Data were collected under conditions of 6 kHz MAS and a temperature of 295 K using a Samoson 7 mm H-X triple-resonance MAS probe head with zirconia rotors and Kel-F® caps. RF pulses with a $4 \mu\text{s}$ length were used with a recycle delay of 140 s. Chemical

shifts were referenced to 1 M YCl_3 .

Spectra were modeled using the simulation program DMFIT;⁴⁴ octahedral ^{27}Al peaks were modeled with Gaussian peaks. Relative populations of ^{27}Al peaks were found by fitting the largest central transition peak and the two nearest spinning sidebands for each signal, then subtracting the average integrated intensity of the two spinning sideband peaks from the integrated intensity of the central peak. The T_1 relaxation times of octahedral ^{27}Al nuclei were found by fixing the peak widths and peak positions of the fit to the single-pulse ^{27}Al data, and fitting the amplitude of the peaks for spectra from each delay time. The integrated intensity curves were then fitted with the curve fitting tool in MATLAB.

Electron Paramagnetic Resonance (EPR) spectroscopy. EPR spectra were collected on a Bruker X-Band EPR spectrometer ($\nu = 9.486$ GHz), equipped with a Helium flow cryostat. Samples were placed in quartz tubes, and data was acquired at temperatures ranging from 4 K to 40 K. The set of linewidths as a function of temperature of the peak at 2480 G were fit with the curve fitting tool in MATLAB. Simulations of the spectra were done using the EASYSPIN code in MATLAB,⁴⁵ with a correction included for field-dependent relaxation effects. The g_x peaks were fit with Gaussian peaks using the program DMFIT.⁴⁴

RESULTS AND DISCUSSION

Dependence of average crystallographic structure on Ce^{3+} substitution. High-resolution synchrotron X-ray diffraction enables the study of small changes in the average structure of ordered materials, and has been used here to accurately probe the effect of the small amount of Ce substitution on the average structure of YAG. Rietveld refinements of synchrotron X-ray data of $\text{Y}_{3-x}\text{Ce}_x\text{Al}_5\text{O}_{12}$ for $x = 0, 0.02, 0.04, 0.06,$ and 0.08 reveal a small, linear increase in the YAG unit cell lattice parameter with Ce^{3+} substitution as seen in Figure 1(b). Such Vegard law behavior suggests all of the Ce^{3+} from the starting materi-

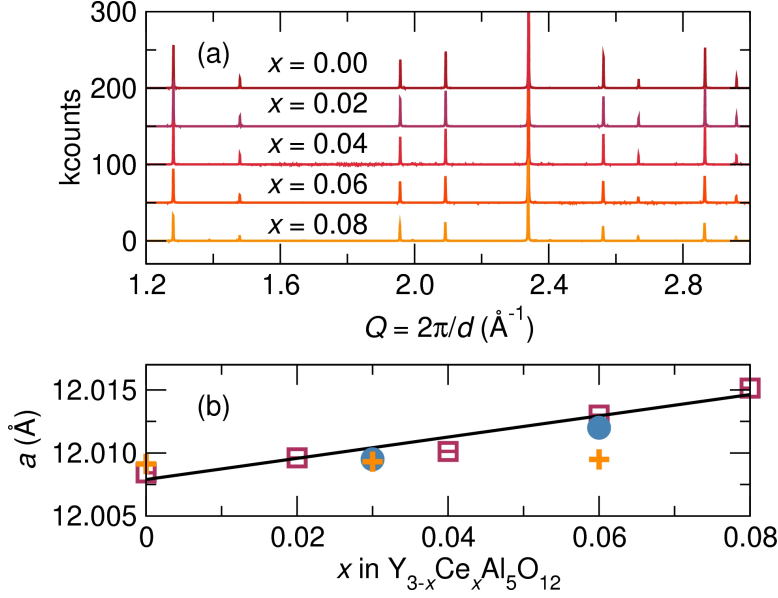


Figure 1. (a) 295 K synchrotron X-ray diffraction patterns of $Y_{3-x}Ce_xAl_5O_{12}$ for x as indicated, and (b) the unit cell parameter from Rietveld refinement as a function of Ce concentration, x . The Vegard law is followed, showing a very small linear expansion of the unit cell with Ce substitution. Orange plus symbols represent data from a 1979 study by Robbins et al.,⁴⁶ and filled light blue circles represent data from a study by Tien et al.¹⁴

Table 1. Crystallographic parameters of $Y_{3-x}Ce_xAl_5O_{12}$ from Rietveld refinement of 11-BM synchrotron X-ray, HIPD neutron, and NPDF neutron scattering data.^a

T (K)	15	15	295	295	295
	$x=0$	$x=0.08$	$x=0$	$x=0.06$	$x=0.09$
Beamline(s)	NPDF	NPDF	11-BM, HIPD	11-BM, HIPD	NPDF
R_p (%)	1.39	1.41	6.17 (X-ray) 1.11 (neut.) 2.27 (overall)	5.74 (X-ray) 1.09 (neut.) 2.19 (overall)	1.49
a (\text{\AA})	11.99067(2)	11.99871(3)	12.008476(3)	12.013001(5)	12.00959(4)
O x	0.280487(3)	0.280487(3)	0.280598(9)	0.28058(1)	0.28062(2)
O y	0.10103(3)	0.10103(3)	0.10092(1)	0.10099(1)	0.10094(2)
O z	0.19914(3)	0.19914(3)	0.199330(9)	0.19946(1)	0.19942(2)
refined Ce_x		0.07(2)		0.09(3)	0.10(1)

^a Ce_x refers to the amount of Ce in $Y_{3-x}Ce_xAl_5O_{12}$. All refinements were done with the $Ia\bar{3}d$ space group (#230). The estimated standard deviations for the last significant digit are given in parenthesis.

als is being substituted into the YAG lattice, and that the expansion of the lattice around Ce is distributed over length scales on the order of the unit cell. The change in unit cell parameter is very small, increasing by only 0.03 % from $x = 0$ to $x = 0.06$ Ce substitution in

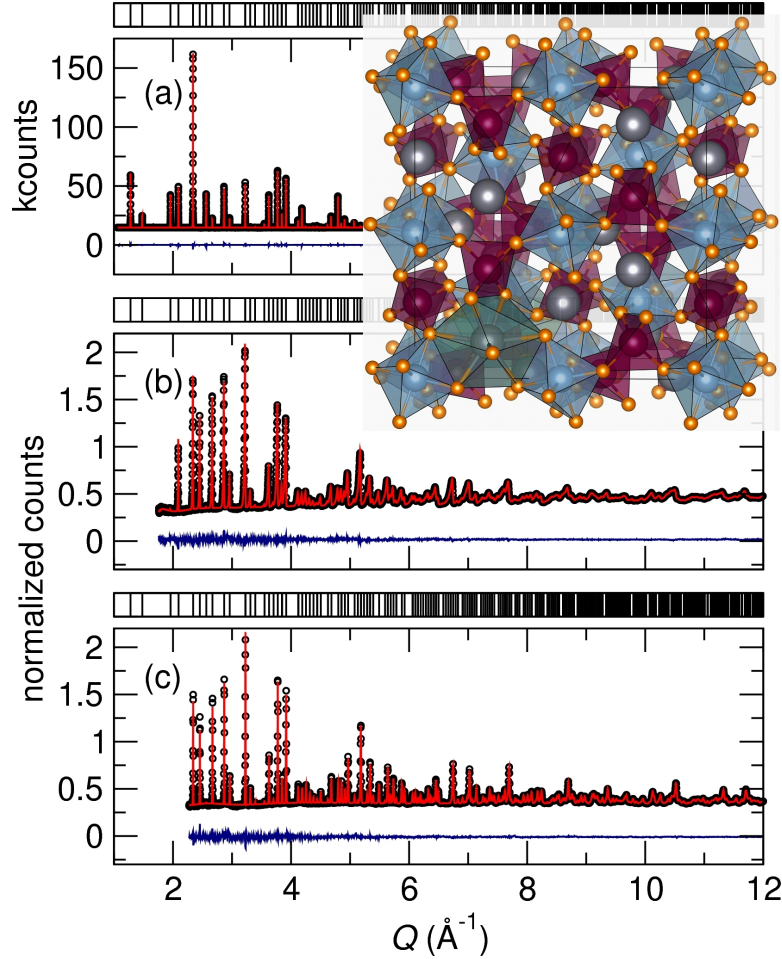


Figure 2. Simultaneous Rietveld refinement of (a) 11-BM synchrotron X-ray and (b) bank 1 HIPD neutron scattering at 295 K of $Y_{2.94}Ce_{0.06}Al_5O_{12}$, and (c) bank 4 NPDF neutron scattering at 15 K of $Y_{2.92}Ce_{0.08}Al_5O_{12}$. The expected reflection positions are shown above each plot. The inset in the upper right shows the YAG structure looking down the a axis, with blue, red, grey, and orange spheres representing octahedral aluminum, tetrahedral aluminum, yttrium, and oxygen atoms, respectively.

$Y_{3-x}Ce_xAl_5O_{12}$. The trend found here is slightly less than a theoretically predicted increase of 0.11% from $x = 0$ to $x = 0.125$ in $Y_{3-x}Ce_xAl_5O_{12}$.²¹ A single-crystal study by Robbins et al. also found a linear increase in the YAG lattice parameter with Ce incorporation.⁴⁶ However, as shown in Figure 1, the expansion of the YAG unit cell parameter found by Robbins et al. is smaller than what was found here, possibly due to less Ce incorporation or resolution limitations/error in the previous study. The trend found here agrees well with another study, which found a linear increase in the unit cell of YAG with Ce incorporation,

prepared using co-precipitation, with Ce substitution of up to $x = 0.18$.¹⁴ The conventional solid-state preparation method used here could not be substituted with more than around $x = 0.09$ with or without flux. This may be due to the low bond valence sums (BVS)⁴⁷ of Al, which are 2.7 and 2.6 for the tetrahedral and octahedral Al sites in the $x = 0$ material, respectively. As Ce is substituted into the YAG lattice, the Al–O bond distances increase. The under-bonding of Al indicated by the BVS, which increases with Ce substitution, may cause the YAG lattice to be unstable past a certain expansion, and may be one reason for the substitution limit of Ce in YAG.

Rietveld refinement of synchrotron X-ray and neutron diffraction data, as shown in Figure 2, yield unit cell parameters, the oxygen position, and Ce occupancy as shown in Table 1. As temperature is decreased from 295 K to 15 K, a very small contraction of about 0.15% in the unit cell and a decrease in atomic displacement parameters (ADPs) are observed. A small change in the unit cell parameter with temperature is consistent with previous measurements of the thermal expansion of YAG, which show the thermal expansion parameter, α , to be on the order of 10^{-6} K^{-1} .⁴⁸ The 295 K NPDF refinement of $\text{Y}_{2.91}\text{Ce}_{0.09}\text{Al}_5\text{O}_{12}$ shows a unit cell that is smaller than expected based on Figure 1(b). Since the neutron data here was collected using time-of-flight methods, Q values come from correlations to the measured time-of-flight of neutrons. This means a small difference from the calibration run to the actual sample run can occur, causing slight differences in the unit cell parameter. The least-squares fit to the PDF of the same NPDF data shows a unit cell parameter in better agreement with Figure 1(b), as discussed later in this paper. The refined occupancy of Ce from the HIPD neutron data gives a result with more Ce than expected [0.09(3) mol % compared to the nominal 0.06 mol %], which does not agree with ²⁷Al NMR results discussed later in this paper. However, the results from the NPDF refinement are within the estimated standard deviation of the nominal values, which agrees well with the ²⁷Al NMR results, indicating that the NPDF instrument may be slightly more sensitive to the Ce in the samples than the HIPD instrument.

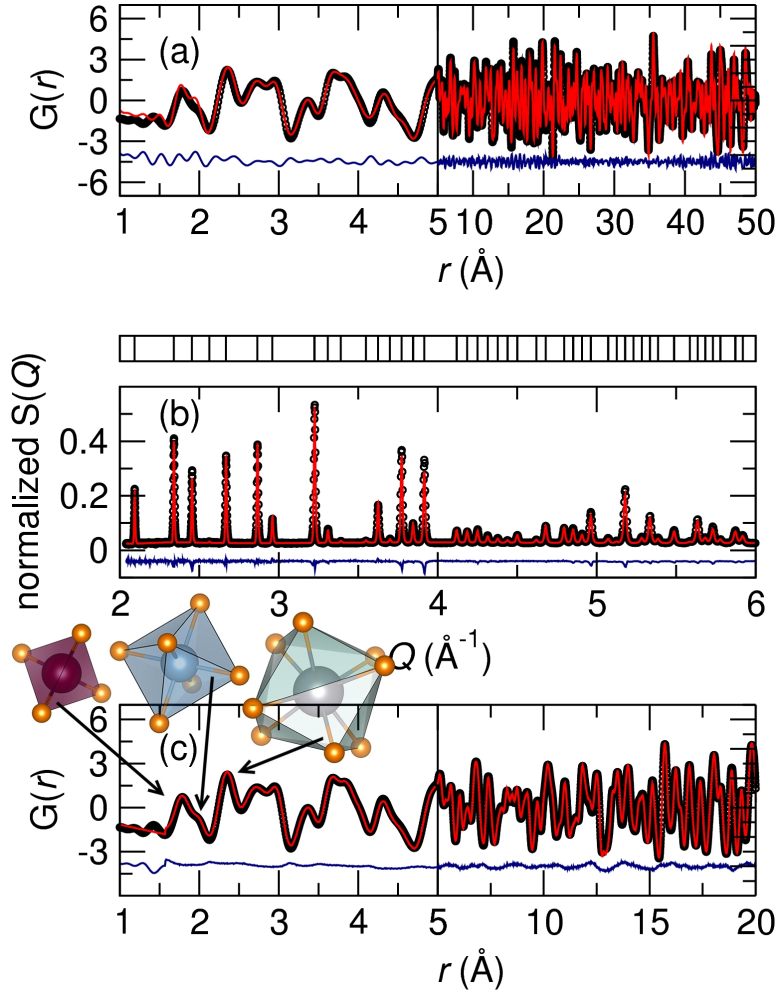


Figure 3. NPDF neutron data taken at 295 K with (a) PDFGUI least-squares fit of $G(r)$, and reverse Monte Carlo fits of (b) $S(Q)$ and (c) $G(r)$ for $\text{Y}_{2.91}\text{Ce}_{0.09}\text{Al}_5\text{O}_{12}$. The expected reflection positions for $S(Q)$ are shown above (b). Polyhedra are shown inset above (c), with arrows denoting the corresponding peaks in the PDF for the (from left to right) tetrahedral Al, octahedral Al, and dodecahedral Y sites.

Local structure around Ce^{3+} from scattering. Rietveld analysis is a powerful tool for investigating the average structure of materials, but it cannot be used to garner information on the local structure of materials since the data represents the structure of a material averaged over many unit cells. Of course, the local structure around Ce in YAG is closely related to the optical properties of YAG:Ce, since the nature of the Ce–O bonds will determine the $5d$ energy levels, and hence, the excitation and emission energies. The PDF, which captures the local and long-range structures of materials through a sine Fourier

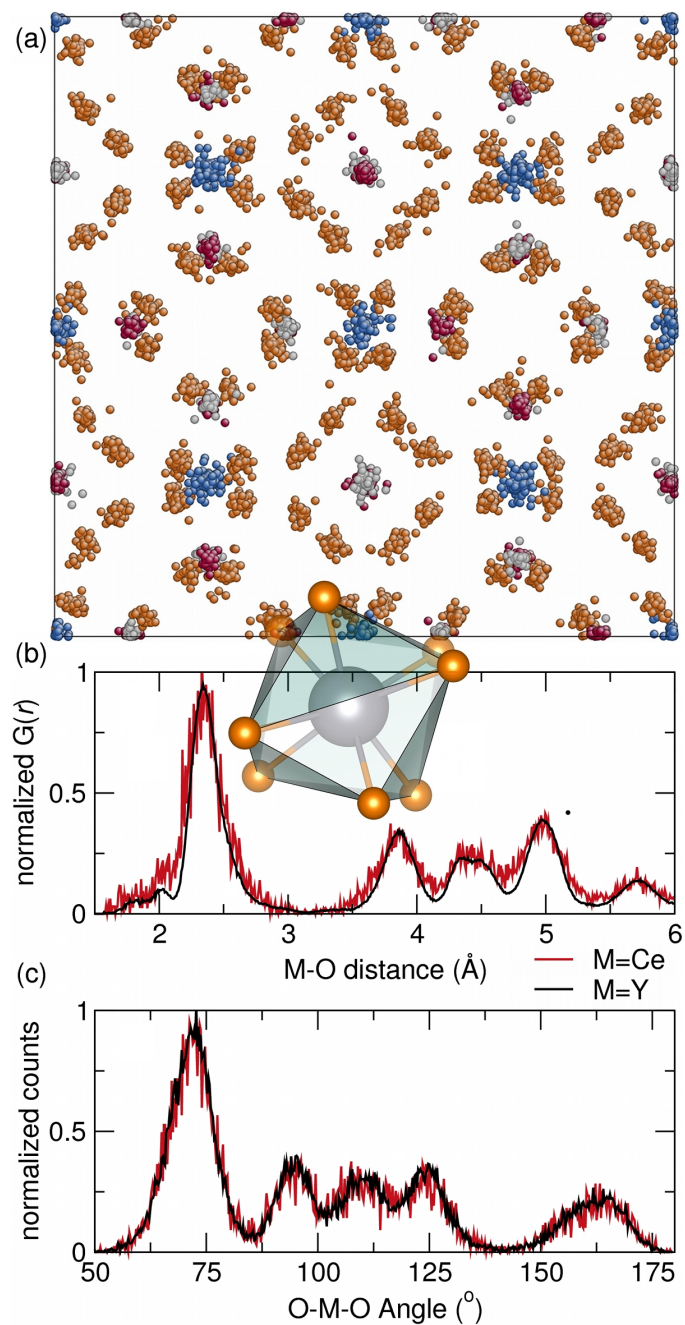


Figure 4. (a) View down the a -axis of the $4 \times 4 \times 4$ RMC supercell of $Y_{2.91}Ce_{0.09}Al_5O_{12}$, fit with 915 moves to NPDF neutron data collected at 295 K, collapsed onto a single unit cell, (b) metal-oxygen distance distributions from the average of 8 reverse Monte Carlo fits of 295 K NPDF neutron data, and (c) oxygen-metal-oxygen bond angle distributions for Y and Ce in $Y_{2.91}Ce_{0.09}Al_5O_{12}$. The inset polyhedron shows a dodecahedral Y-O polyhedron from the average YAG structure. Blue, red, grey, and orange spheres in (a) represent octahedral aluminum, tetrahedral aluminum, yttrium, and oxygen atoms, respectively.

transform of Bragg scattering, gives local structure information that is complementary to a Rietveld analysis. One way to compare the average structure from Rietveld refinement to the local structure from total neutron scattering is by fitting the PDF with a least-squares method using a periodic unit cell in PDFGUI.³⁵ The PDFGUI least-squares fit to the 295 K PDF of $\text{Y}_{2.91}\text{Ce}_{0.09}\text{Al}_5\text{O}_{12}$ out to 50 \AA , shown in Figure 3(a), fits the data well with a R_{wp} of 13.9%. The Rietveld analysis of the $S(Q)$ data for $\text{Y}_{2.91}\text{Ce}_{0.09}\text{Al}_5\text{O}_{12}$ ($R_{wp} = 1.49\%$) yields a cell parameter of 12.010 \AA , considerably smaller than the result from a least-squares fit of the PDF to 50 \AA in PDFGUI of 12.017 \AA , which is in good agreement with what is expected from Figure 1(c). The Rietveld unit cell is smaller likely due to the time-of-flight correlation, which is fitted based on a standard material, such as silicon; however, this correlation can differ slightly from run to run depending on the exact sample placement, and is likely the reason for the smaller obtained unit cell from Rietveld analysis.

The limitations of least squares refinement of PDF data using a periodic unit cell, as in PDFGUI, can be overcome by using reverse Monte Carlo (RMC) simulations, which simultaneously models the local and long-range structure of a material without symmetry constraints.^{36,37,49,50} Since Y and Ce have sufficiently different neutron scattering lengths (4.03 barn and 7.15 barn for Ce and Y, respectively), Ce can be distinguished from Y in the simulations, allowing for investigation of the local structure around Ce in YAG. Comparison of a simulation of YAG:Ce with Y in place of Ce shows that the fit is slightly improved by using Ce instead of Y in the simulation (χ^2 of 3.55 compared to 3.57 for simulations with Ce and with only Y used, respectively). The result of the RMC fits to the data are shown in Figure 3(b),(c), and the super cell of $4 \times 4 \times 4$ unit cells is shown collapsed onto one unit cell in Figure 4(a).

Any histogram of atom-atom distances can be extracted from the fit, but the most useful information lies within the local environment of Ce compared to the Y in the structure, for which the Ce–O and Y–O distance histograms are shown in Figure 4(c). The results from the RMC simulation of $\text{Y}_{2.91}\text{Ce}_{0.09}\text{Al}_5\text{O}_{12}$ shows the Ce–O distance histogram and

O–Ce–O bond angle histograms are the same as the Y–O distance histogram and O–Y–O bond angle histograms. The average BVS^{47,51} from the Ce–O bond distance histogram is 4.0 ± 0.1 , much higher than the nominal valence state of 3, and the BVS of Y, which is around 3.1 ± 0.1 . This implies that Ce^{3+} is severely compressed in the YAG lattice, since the Shannon-Prewitt ionic radii of 8-coordinate Ce^{3+} (1.143 \AA) is much larger than 8-coordinate Y^{3+} (1.019 \AA).⁵² The compression leads to a large crystal field splitting of the Ce $5d$ states in YAG, since short Ce–O bond distances lead to large crystal field splittings.⁹ This results in the blue absorption and yellow emission that has been observed, consistent with previous observations of an unusually large crystal field splitting in YAG:Ce.¹⁰ The average Ce–O distances of 2.31 \AA and 2.44 \AA found here are slightly less than those from the EXAFS results as discussed later in this paper, which show the Ce–O bond distances to be $2.40(2) \text{ \AA}$ and $2.50(2) \text{ \AA}$, but are within the error of the measurements since the uncertainty is around 0.1 \AA in the PDF and EXAFS measurements. The nearly imperceptible distortion of the lattice around Ce^{3+} is consistent with the small increase in unit cell parameter found from Rietveld analysis in Figure 1(b), since a larger local distortion around Ce would be expected to expand the lattice by a greater amount.

The RMC simulation results also show a random distribution of Ce–Ce distances, indicating a random distribution of Ce in the lattice. This is consistent with the ²⁷Al NMR and EPR results, which, as discussed later in this paper, show that Ce^{3+} ions are randomly distributed in the YAG lattice.

Total neutron scattering offers a unique way to investigate the local structure around Ce^{3+} in YAG:Ce free from symmetry constraints, but EXAFS is an even more selective probe for investigating the local structure of Ce in YAG. Simultaneously, the oxidation state of the Ce atoms in YAG:Ce, which is of utmost importance to its optical properties since Ce^{4+} ions have been known to quench Ce^{3+} luminescence,⁵³ has been probed with XANES. The XANES data collected on $\text{Y}_{2.91}\text{Ce}_{0.09}\text{Al}_5\text{O}_{12}$ at 295 K, shown in Figure 5(a), reveals the Ce absorption edge lies at 40.469 keV , a lower energy than the Ce absorption edge in CeO_2 at

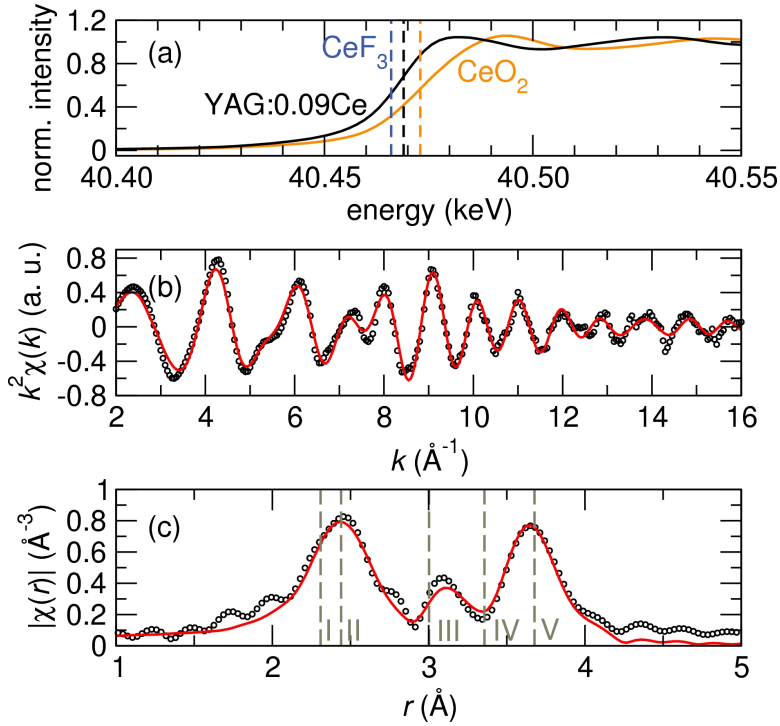


Figure 5. Ce K-edge (a) XANES spectra of $\text{Y}_{2.91}\text{Ce}_{0.09}\text{Al}_5\text{O}_{12}$ and CeO_2 , (b) $k^2\chi(k)$ data and fit, and (c) $\chi(r)$ data and fit collected at 295 K. The vertical dashed lines in (a) indicate the absorption edges for CeF_3 at 40.466 keV,³⁹ $\text{Y}_{2.91}\text{Ce}_{0.09}\text{Al}_5\text{O}_{12}$ at 40.469 keV, and CeO_2 at 40.473 keV.³⁹ The vertical dashed lines in (b) indicate the Y-X (X = O, Al, Y) interatomic distances from Rietveld refinement of 295 K NPDF data of the same sample, with I, II, III, IV, and V corresponding to Y-O1, Y-O2, Y-Al(4), Y-Al(6), and Y-Al(4)/Y distances, respectively. A phase shift was applied to the data and fit in (c) based on the first Ce-O coordination shell.

40.473 keV, but a higher energy than Ce in CeF_3 at 40.466 keV.³⁹ This result shows that the Ce in YAG is indeed in the 3+ state, as is crucial for the optical properties. It also confirms the ^{27}Al NMR result that all Ce in these materials is in the 3+ state, as discussed later in this paper. The higher absorption edge of $\text{Y}_{2.91}\text{Ce}_{0.09}\text{Al}_5\text{O}_{12}$ compared to CeF_3 is likely due to the nature of fluoride versus oxide lattices.

A fit to the EXAFS data shown in Figure 5(b),(c) (R -factor of 1.55%) reveals that even with relatively high concentrations of Ce in $\text{Y}_{3-x}\text{Ce}_x\text{Al}_5\text{O}_{12}$ ($x = 0.09$ in this case), the lattice locally distorts by the same amount as was observed with lower concentrations of Ce ($x = 0.03$) in another EXAFS study.²² The 2 Ce-O distances of 2.40(2) Å and 2.50(2) Å agree well with previous findings of 2.38(1) Å and 2.52(2) Å,²² theoretical predictions of

Table 2. Inter-atomic Ce–X distances for $Y_{2.91}Ce_{0.09}Al_5O_{12}$ from Rietveld refinement of 295 K NPDF data compared with those from the fit to 295 K 20-BM EXAFS data.^a

X	N	Ce–X distance (Å)	
		Rietveld	EXAFS
O1	4	2.3090(2)	2.40(2)
O2	4	2.4401(2)	2.50(2)
Al(4)	2	3.00238(2)	3.05(1)
Al(6)	4	3.35677(2)	3.41(1)
Al(4)	4	3.67715(2)	3.71(1)
Y	4	3.67715(2)	3.71(1)

^a The EXAFS fit also included the next 2 coordination shells around Ce (Ce–O pairs), but the distances did not differ significantly from the Rietveld refinement. The estimated standard deviations are shown in parenthesis for the last significant digit.

2.373 Å and 2.468 Å,²¹ and the RMC results, but are slightly larger compared to the values from one ab-initio study of 2.370 Å and 2.441 Å.²⁰ The small 3% expansion of Ce–O bond distances compared to the average structure Y–O distances allows the BVS^{47,51} to decrease from 4.0 ± 0.1 to 3.3 ± 0.1 . This indicates that while Ce is tightly compressed in the YAG:Ce lattice, a small expansion of the local bond lengths dramatically decreases the BVS to a more reasonable value.

The higher resolution here compared to the previous EXAFS study of YAG:Ce²² enables a more precise investigation of the Al and Y atoms near Ce in the structure, and reveals that the Ce–Al and Ce–Y distances in the first few Ce coordination shells do in fact significantly deviate from the average structure Y–Al and Y–Y distances. This shows that the distortion around Ce³⁺ ions in YAG is not limited to the first coordination shell of O and Al atoms, but in fact spans many coordination shells. This is a more satisfying explanation as to why the lattice expands with addition of Ce—the distortions are not contained within a short

distance, but are spread out over the structure. This 3% change in the first coordination sphere of Ce–O translates to an expansion of the unit cell on the order of 0.01% seen in the synchrotron X-ray results, due to spreading of the distortion over the YAG lattice. Past the Ce–Y coordination shell at around 3.7 Å, the distortions become imperceptible to the EXAFS measurement. However, it is anticipated from the Rietveld analysis that these distortions do exist in smaller amounts as distance from a Ce ion increases.

Table 3. Isotropic atomic displacement parameters of $Y_{3-x}Ce_xAl_5O_{12}$ from Rietveld refinement and PDFGUI (least-squares fit to the PDF) fits of neutron and X-ray scattering data.^a

T (K)	15	15	295	295	295	295	295
	$x=0$	$x=0.08$	$x=0$	$x=0.06$	$x=0.09$	$x=0.09$	$x=0.09$
data type	NPDF	NPDF	HIPD neutron	HIPD neutron	NPDF	NPDF	
method	Rietveld	Rietveld	11-BM X-ray	11-BM X-ray	Rietveld	PDFGUI (1 Å to 50 Å)	EXAFS
Y/Ce B_{iso} (Å ²)	0.16(1)	0.20(1)	0.178(3)	0.227(4)	0.36(1)	0.43(6)	0.36(4)
Al(6) B_{iso} (Å ²)	0.12(1)	0.20(1)	0.215(4)	0.250(5)	0.33(1)	0.38(4)	0.2(1)
Al(4) B_{iso} (Å ²)	0.19(3)	0.23(2)	0.21(1)	0.22(1)	0.34(2)	0.39(2)	0.2(1)/0.36(4) ^b
O B_{iso} (Å ²)	0.25(1)	0.30(1)	0.255(5)	0.295(6)	0.43(1)	0.51(6)	0.36(4)
θ_D (K)	634	506	853	760	628	578	690

^a Estimated standard deviations for the last digits of parameters are given in parenthesis. All refinements used the $Ia\bar{3}d$ space group (#230). The numbers reported for the EXAFS fit are mean-square relative displacement factors. The Debye temperatures shown, θ_D , are the average of the values calculated from the isotropic atomic displacement parameters.⁵⁴

^b The two atomic displacement parameters are for the 3rd and 5th coordination shells around Ce, respectively.

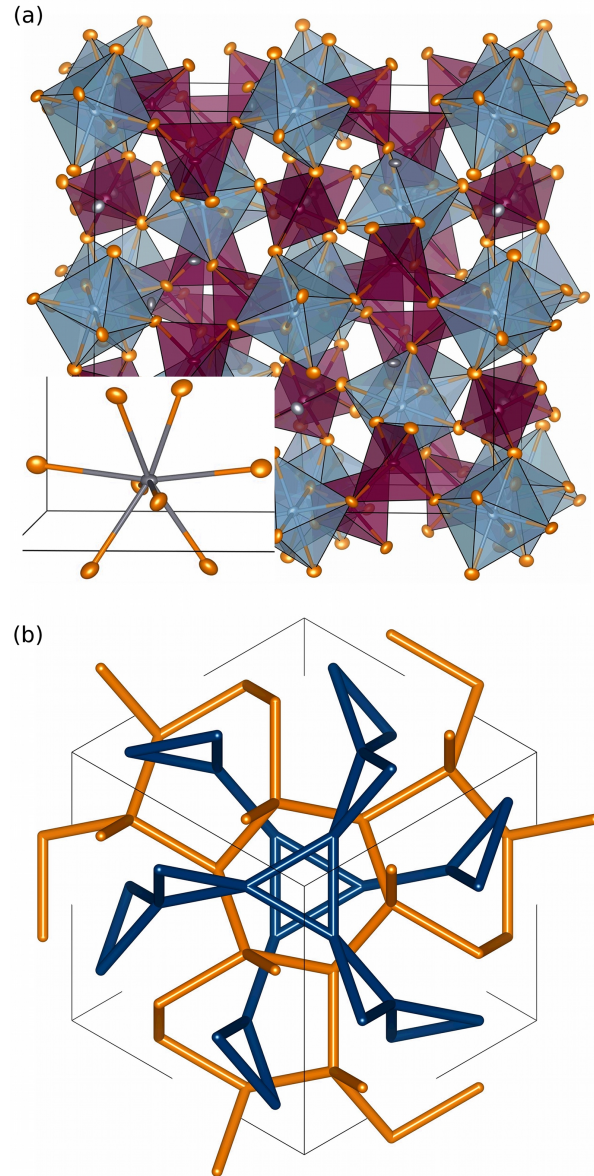


Figure 6. (a) View down the a -axis of the Rietveld-refined structure of $\text{Y}_{2.94}\text{Ce}_{0.06}\text{Al}_5\text{O}_{12}$ at 295 K from 11-BM synchrotron X-ray data and HIPD neutron data, with the inset showing an expanded view of a Y atom with bonds drawn to the surrounding O atoms. 99% probability atomic displacement parameters are shown by blue, red, grey, and orange ellipsoids, which represent octahedral aluminum, tetrahedral aluminum, yttrium, and oxygen atoms, respectively. (b) View down the (111) face of the YAG unit cell, showing the inter-penetrating networks of Y and Al, which form a double-gyroid structure. The blue cylinders are drawn between Y atoms, while the orange cylinders connect tetrahedral Al atoms. The octahedral atoms were excluded for clarity.

The rigid YAG lattice is related to its high quantum efficiency. Whereas the X-rays used earlier in this paper to accurately determine the unit cell have a form factor that

decays rapidly with increasing Q , neutron scattering intensities essentially remain flat with increasing Q , enabling a precise investigation of the atomic displacement parameters.⁵⁵ A simultaneous Rietveld refinement of synchrotron X-ray and neutron scattering therefore yields a structural model of a material that accurately represents the long-range order and ADPs. As shown in Table 3, increasing Ce concentration correlates with increasing ADPs. This is due to greater disorder in the structure, due to distortions from the substituted Ce ions, as well as an increase in the low-frequency phonon modes due to the addition of heavier Ce atoms into the structure. The least-squares PDFGUI fit to the PDF out to 50 Å gives larger isotropic ADPs than the Rietveld fit, which is due to the inclusion of the local and long-range structure in the same refinement. The small ADPs from Table 3 are related to the high quantum efficiency of YAG:Ce of around 90% (the anisotropic displacement parameters can be found in the supporting information, Table S1).

The ADPs found here, shown for the unit cell from $Y_{2.94}Ce_{0.06}Al_5O_{12}$ with 99% probability in Figure 6(a), are slightly less than those of yttrium-aluminum perovskite⁵⁶ and $MgAl_2O_4$,⁵⁷ and about half of those of cerium-aluminum perovskite.⁵⁸ The small ADPs indicate a high degree of crystalline order and small thermal motions of atoms, and decrease with decreasing temperature as expected. This coincides with the increase of quantum efficiency at low temperature,¹² supporting the relationship between small ADPs and high quantum efficiency. The mean-square relative displacements (MSRDs) from the EXAFS fit are much smaller than the ADPs found from Rietveld analysis of the same sample; the ADPs from Rietveld and MSRDs of the EXAFS converge as the distance from Ce increases. Of course, caution must be taken when comparing ADPs to MSRDs, since the MSRDs include correlated atomic motions. The smaller MSRDs from the EXAFS fit are the result of the large size of Ce in the lattice, which diminishes the amount of space available for nearby atoms to vibrate.

The tight compression of Ce in YAG seen in the RMC and EXAFS results is related to the small MSRDs near Ce, which relates to the low probability of non-radiative transitions

and high quantum efficiency. Small MSDs around substituted Ce ions decrease the accessible phonon energy levels that aid in quenching excited Ce^{3+} electrons non-radiatively, thereby decreasing the probability of non-radiative transitions.⁹ A relationship between high quantum efficiency and small ADPs is also supported by the Debye temperature. The relationship between Debye temperature (θ_D), which gives an estimate of the temperature at which the highest frequency vibrational mode of a crystal is excited,⁵⁴ and the average atomic displacement shows how less phonon modes are accessible at a given temperature in a rigid lattice compared to a floppy lattice. For example, the average U_{iso} measured here for YAG at 295 K is around 0.0093 \AA^2 , corresponding to the previously measured $\theta_D = 760 \text{ K}$.⁵⁹ Another crystal structure, $\text{KGd}(\text{WO}_4)_2$, with a lower θ_D of 580 K,⁵⁹ has an average U_{iso} measured as 0.020 \AA^2 ,⁶⁰ indicating that at a given temperature more phonon modes will be populated in $\text{KGd}(\text{WO}_4)_2$ compared to YAG.

The small isotropic ADPs can in fact be used to calculate the Debye temperature,⁵⁴ and as shown in Table 3, the Debye temperatures calculated in this fashion are typically less than the literature value of 760 K in the low-temperature limit, and greater than the literature value in the high-temperature limit. The high temperature limit involves an assumption that the measurement temperature is greater than θ_D , which is not valid in our case and explains the discrepancy. The low-temperature limit result for $x = 0$ is much less than the reported value of 760 K, which agrees with the typical trend of results for other crystal structures in literature,⁶¹ but may also be due to static disorder in the samples. As Ce is added to the lattice, θ_D decreases, indicating that more vibrational modes are accessible at a given temperature. This is consistent with the larger mass of Ce, which is expected to increase the number of low-frequency Einstein modes available to the system. Non-radiative transitions, which decrease the quantum efficiency, can occur due to vibronic coupling and other phenomena associated with disorder and large amounts of vibrations near activator ions.⁹ The decreasing θ_D should therefore correlate with an increase of non-radiative transitions, and decreased quantum efficiency. Till now, a decrease

in quantum efficiency with increasing activator ion content has been attributed to energy transfer between activator ions, but appears to also result from an increased amount of accessible phonon modes at a given temperature. The smaller MSRDS from the EXAFS fit result in an even smaller calculated θ_D compared to the θ_D from Rietveld refinement ADPs, indicating that Ce locally sees a higher Debye temperature. This indicates that, overall, less phonon modes are accessible at a given temperature near Ce compared to other parts of the YAG lattice. This would decrease the non-radiative recombination pathways of a Ce^{3+} ion in the excited state, further supporting the relationship between small ADPs/MSRDS and high quantum efficiency in phosphors.

The rigid lattice exhibited by YAG is of course closely related to its structure. The Y–Y and Al–Al connectivity forms a double-gyroid structure though Y–O–Y and Al(4)–O–Al(6)–O–Al(4) pathways, shown as a simplified version of Y–Y and Al(4)–Al(4) connectivities in Figure 6(b). The Al(4) and Al(6) network is formed by corner sharing of the Al polyhedra, which would not typically happen with something with a higher charge and similar coordination numbers, such as tetrahedral Si, per Pauling’s fourth rule of determining the structure of ionic crystals.⁶² The high connectivity of the YAG lattice decreases the degrees of freedom available for phonon modes, especially local Einstein-like modes, leaving few vibrational modes to aid in non-radiative transitions of the unpaired Ce^{3+} electron from the $5d$ to the $4f$ state.

Probing the local structure around Ce^{3+} by utilizing its spin effects on proximal ^{27}Al and ^{89}Y nuclei. Structural reasons for the high quantum efficiency of YAG:Ce can also be probed by spectroscopic methods, which offer a means to investigate materials in a way that is complementary to scattering methods. For example, solid-state NMR spectroscopy can be used to accurately quantify nuclei by phase or crystallographic site in a material, which can be compared to results from scattering. NMR also enables selective investigation of the local electronic environment of one particular nucleus, while conven-

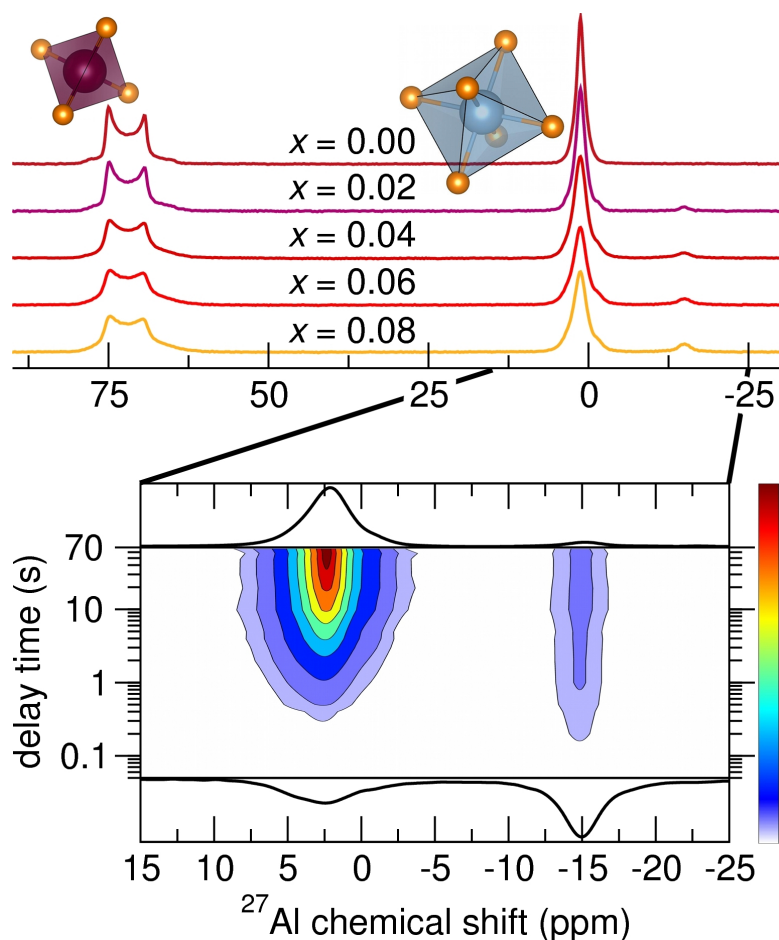


Figure 7. (a) Single-pulse solid-state ^{27}Al NMR spectra (24 kHz MAS) of $\text{Y}_{3-x}\text{Ce}_x\text{Al}_5\text{O}_{12}$ taken at 295 K and 18.8 T with varying amounts of Ce^{3+} substitution in $\text{Y}_{3-x}\text{Ce}_x\text{Al}_5\text{O}_{12}$ as indicated. The small signal near -15 ppm is from octahedral ^{27}Al nuclei near substituted Ce. (b) Solid-state ^{27}Al NMR saturation recovery spectra (14 kHz MAS) on the octahedral ^{27}Al signals of $\text{Y}_{2.94}\text{Ce}_{0.06}\text{Al}_5\text{O}_{12}$ at 295 K and 11.7 T, showing that the -15 ppm signal saturates much faster (has a shorter T_1 relaxation time) than the bulk octahedral signal. Contour lines are at relative intensity levels of 0.1, 0.2, 0.5, 1, 1.5, 2.0, 2.5, 3.0, and 3.3.

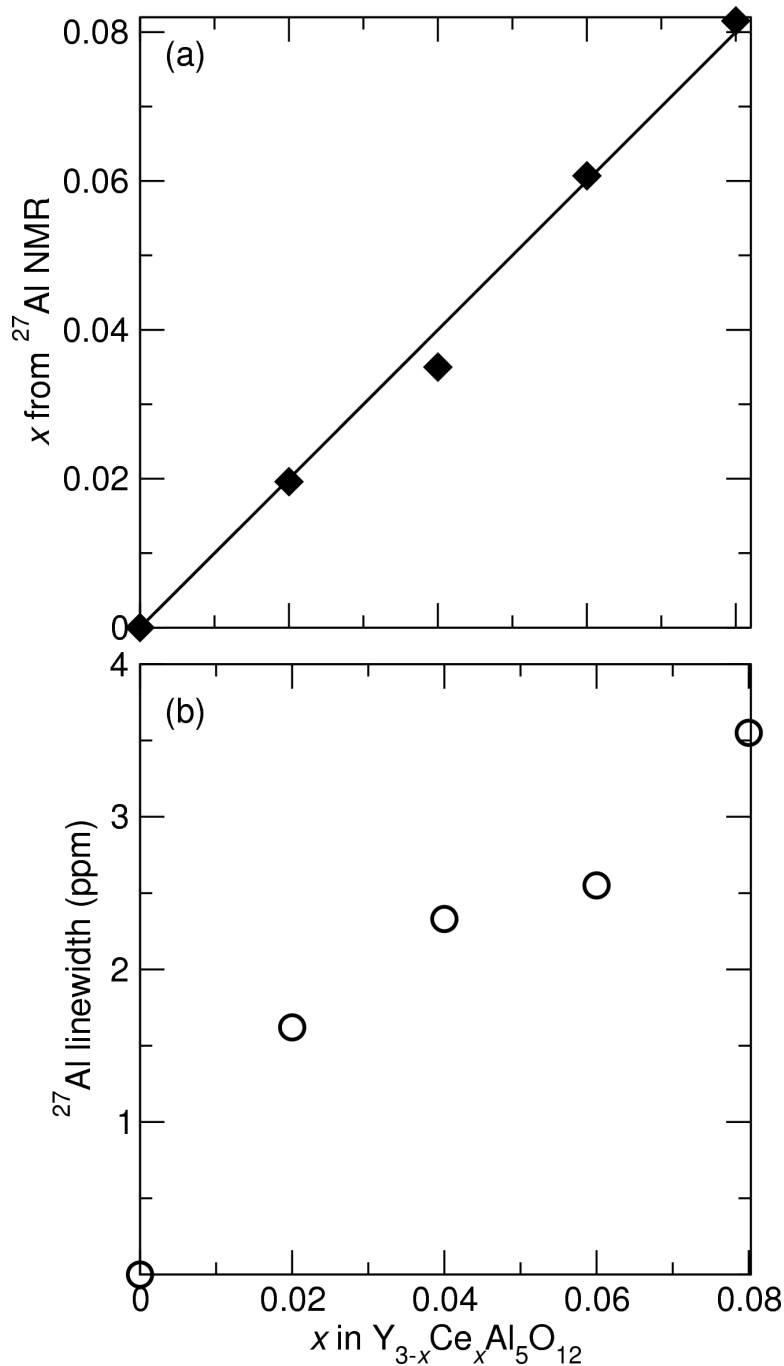


Figure 8. (a) Cerium composition in $Y_{3-x}Ce_xAl_5O_{12}$ as calculated from fits to 1D single-pulse solid-state ^{27}Al MAS NMR spectra and (b) FWHM (Γ , open circles) from the same fits. The line in (a) is the $y = x$ line of Ce composition, x . Ce concentration, x , was found from the fits by taking the relative integrated intensity of the octahedral ^{27}Al compared to the entire octahedral ^{27}Al region and dividing by 4 (for the number of ^{27}Al nuclei in the first coordination sphere around Ce), and multiplying by 3 to normalize for the nominal composition, $Y_{3-x}Ce_xAl_5O_{12}$.

tional scattering methods must probe all atoms in a material at once. In YAG:Ce, the 100% naturally abundant ^{27}Al and ^{89}Y nuclei enable such a selective, quantitative analysis that provides unique information complementary to the scattering and XANES/EXAFS results. The unpaired electron in the $4f$ shell of Ce^{3+} alters the local magnetic field of nearby nuclei, enabling a selective probe of the YAG lattice around the Ce^{3+} dopant ions. The 1D single-pulse ^{27}Al spectra in Figure 7(a) of $\text{Y}_{3-x}\text{Ce}_x\text{Al}_5\text{O}_{12}$ with $x = 0, 0.02, 0.04, 0.06,$ and $0.08,$ shows the resolved ^{27}Al signals located at 77 ppm and 1.3 ppm, associated with the tetrahedral and octahedral ^{27}Al sites, respectively. These results confirm that the samples are highly crystalline and single-phase, and are in good agreement with previous measurements of undoped YAG.^{63,64} As Ce is added, broadening of both signals is observed, and a second octahedral signal appears near -15 ppm. The relative integrated signal intensities of the two types of ^{27}Al signals from all samples agree well with the expected 3:2 ratio for the tetrahedral:octahedral ^{27}Al nuclei in YAG, including the signal near -15 ppm in the octahedral ^{27}Al population. This signal near -15 ppm has been previously regarded as an impurity,⁶⁵ but is in fact the signal from the first coordination sphere of ^{27}Al nuclei near paramagnetic Ce^{3+} in YAG:Ce, supported by an increase in intensity with increasing Ce concentration. This has never before been reported in cerium-doped YAG, though displacement and broadening of ^{27}Al and ^{89}Y NMR spectra due to substitutions of rare-earth ions has been observed in the past in YAG:Tb,⁶⁶ stannates,⁶⁷ and pyrochlores.⁶⁸ Materials prepared with or without BaF_2 and NH_4F fluxes yielded nearly identical 1D single-pulse solid-state ^{27}Al MAS NMR spectra as shown in supporting information Figure S2(a), showing that the local environment of Ce is not affected by the use of BaF_2 and NH_4F flux in the preparation. This observation suggests Ba does not substitute into the lattice in substantial amounts, consistent with the large energy (from DFT calculations) associated with Ba substitution on the Y site of around 5 eV.⁶⁹

Calculation of the Ce concentration from the relative integrated intensities of the -15 ppm signal shown in Figure 8(a) reveals a linear increase in the amount of octahedral ^{27}Al nu-

Table 4. Ce–X distances from the HIPD/11-BM 295 K Rietveld refinement, with parameters from fits to the ^{27}Al and ^{89}Y NMR spectra for $\text{Y}_{2.94}\text{Ce}_{0.06}\text{Al}_5\text{O}_{12}$.^a

Atom	Coord. shell	Number of nuclei	Ce–X r (Å)	Calculated δ_{iso} (ppm)	Fitted δ_{iso} (ppm)	Γ (ppm)	T_1 (s)	Population (%)
6-coord.	bulk				1.26	2.14	6.55	71.5
^{27}Al	1	2	3.36	–27.2	–15.0	2.52	0.318	4.25
	1	2	3.36	21.6	–15.0	2.52	0.318	4.25
	2	2	5.41	6.1	3.15	2.12	2.44	4.0
	2	2	5.41	1.7	bulk ^b	bulk ^b		
	3	4	6.88	–1.7	–1.18	2.29	5.82	7.9
	3	4	6.88	2.3	3.15	2.12	2.44	8.1
4-coord.	bulk				77			86.9
^{27}Al	1	2	3.00	105.4	71.6			4.3
	2	2	3.68	61.5	71.6			4.3
	2	2	3.68	84.7	79.2			4.5
	3	2	5.62	80.4	bulk ^b			
	3	2	5.62	73.0	bulk ^b			
	3	4	5.62	77.7	bulk ^b			
^{89}Y	bulk				222	2.6		67.0
	1	2	3.68	206	237	2.9		5.5
	1	2	3.68	229	237	2.9		5.5
	2	2	5.62	225	225	2.1		5.5
	2	2	5.62	218	212	2.0		11.0
	2	4	5.62	223	bulk ^b			
	3	2	6.00	226	225	2.1		5.5

^a The calculated paramagnetic displacement (δ_{iso}) was obtained from Equation 1, fitted displacements of octahedral/tetrahedral ^{27}Al and ^{89}Y , FWHM (Γ), and populations are from fits to the data using DMFIT, and T_1 relaxation times were measured from saturation-recovery experiments. The octahedral ^{27}Al peaks were modeled with Gaussian peaks.

^b "Bulk" indicates the signal was assumed to coincide with the bulk signal.

clei in the first coordination sphere around substituted Ce, which matches the nominal compositions. This indicates that all the Ce in the starting materials has been incorporated into the YAG lattice, in agreement with the 11-BM synchrotron X-ray Rietveld refinement results, which showed linear expansion of the unit cell with Ce incorporation. Additionally, for the displacement of the octahedral ^{27}Al NMR signal to occur, Ce must be in the 3+ state so that it is paramagnetic. Therefore, the quantitative results in Figure 8(a) also demonstrate that all of the Ce in the lattice must be in the 3+ state, corroborating the XANES result. The full width at half maximum (Γ) values in Figure 8(b) show a linear increase with Ce content, indicating a larger amount of inhomogeneity in the local electronic environment of the octahedral ^{27}Al nuclei nearest Ce with increasing Ce substitution. Finally, since the paramagnetic shift of the signal from octahedral ^{27}Al sites in close proximity to Ce^{3+} is additive with the amount of Ce nearby, a ^{27}Al nucleus near 2 Ce^{3+} ions would resonate around -30 ppm.^{67,68,70} The signal around -30 ppm from such ^{27}Al nuclei is only discernible from the noise in the spectrum of the $x = 0.08$ material since the relative population of this peak is very small. Quantification of the spectra from the $x = 0.08$ material results in about 0.44% of octahedral Al in the material being found near 2 Ce^{3+} ions, in good agreement with the 0.40% expected in a random distribution of Ce^{3+} in the lattice. This result agrees well with the RMC result, which showed a random distribution of Ce in the YAG lattice.

The displacement of octahedral ^{27}Al signals due to proximal Ce^{3+} ions is a result of through-bond sharing of the Ce^{3+} 4*f* electron spin density with the surrounding lattice (the Fermi "contact" shift) and/or a through-space dipolar interaction ("pseudocontact" shift) between the unpaired Ce^{3+} 4*f* electron with the ^{27}Al unpaired nuclear spins.^{68,71} The equation for fractional shift in nuclear resonance frequency due to the dipolar contribution is⁷⁰

$$\frac{\Delta\nu}{\nu_0} = \frac{-g^2\beta^2J(J+1)(2J-1)(2J+3)F}{60(kT)^2r^3}, \quad (1)$$

where

$$F = A_2^0 \langle r^2 \rangle (3 \cos^2 \theta - 1) \langle J \| \alpha \| J \rangle. \quad (2)$$

The terms $g = 6/7$, $J = 5/2$, and $\langle J \| \alpha \| J \rangle = -0.0571$ are constants specific to Ce^{3+} .⁷⁰ The value $A_2^0 = -159 \text{ cm}^{-1}$ is a crystal field parameter for Ce^{3+} in YAG,⁷² and the value of $\langle r^2 \rangle$ for the $\text{Ce}^{3+} J = 5/2$ state is 1.193 (in atomic units).⁷³

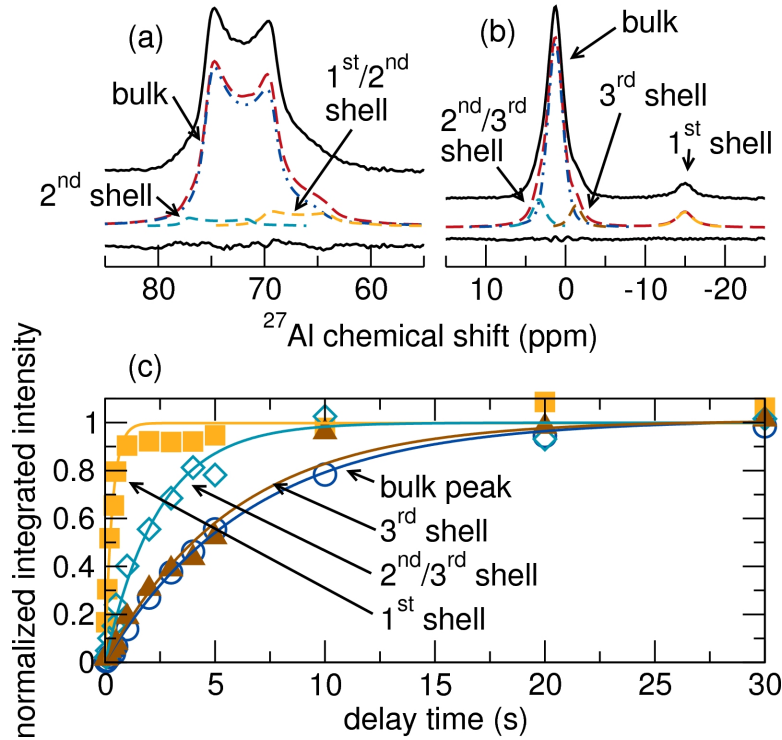


Figure 9. Fits to the (a) tetrahedral and (b) octahedral components of the 1D single-pulse solid-state ^{27}Al NMR spectra (24 kHz MAS) of $\text{Y}_{2.94}\text{Ce}_{0.06}\text{Al}_5\text{O}_{12}$ taken at 295 K and 18.8 T. The fits have been offset from the data for clarity. (c) Normalized integrated intensities of ^{27}Al signals from the bulk, 1st, 2nd, and 3rd coordination shells around substituted Ce^{3+} from the saturation-recovery experiment shown in Figure 7(b). The solid lines show the exponential fit to the data (integrated intensity = $M_z^0(1 - e^{-t/T_1})$). The T_1 relaxation time decreases with decreasing ^{27}Al - Ce^{3+} distance, indicating increasing ^{27}Al - Ce^{3+} interaction strength with decreasing distance.

The internuclear distances from the HIPD/11-BM 295 K Rietveld fit along with predicted and actual (fitted) isotropic chemical shifts from Equation 1 are tabulated in Table 4. The octahedral ^{27}Al nuclei nearest a substituted Ce^{3+} is predicted to be displaced

in both the positive and negative directions from Equation 1, since these ^{27}Al nuclei are at differing angles from the anisotropic Ce^{3+} unpaired electron spin density. However, this signal is only shifted in the *negative* direction to -15 ppm from the bulk signal around 1 ppm. This indicates that the primary source of the displacement is the Fermi "contact" shift, which is consistent with a de-localization of the Ce^{3+} $4f$ spin density with the nearest octahedral ^{27}Al nuclei. Equation 1 successfully predicts the direction of the displacements of the next two coordination spheres of octahedral ^{27}Al around a substituted Ce^{3+} ion. This indicates that the Fermi "contact" shift plays a significant role for only the first coordination sphere of octahedral ^{27}Al around Ce^{3+} , and dipolar interactions ("pseudocontact" interactions) dominates the second and further coordination spheres of octahedral Al near Ce^{3+} .

Figure 9(a),(b) shows the excellent fits to the single-pulse ^{27}Al NMR spectra obtained using these predicted displacement values for $\text{Y}_{2.94}\text{Ce}_{0.06}\text{Al}_5\text{O}_{12}$, similar results are obtained for the other single-pulse ^{27}Al spectra. The population of the ^{27}Al nuclei corresponding to the -15 ppm signal amounts to 4 times the Ce concentration in the sample. This is consistent with the first coordination shell of Al atoms around Ce, which contains 4 Al atoms equidistant to Ce (see Table 4). Integration of the signals at 1.3 ppm, 3.2 ppm, -1.2 ppm, and -15 ppm yields populations of 71.5 : 12.1 : 7.9 : 8.5, meaning that the largest displaced signal (corresponding to 12% of the population at 3.2 ppm) is a mixture of the second and third coordination spheres of ^{27}Al nuclei around Ce^{3+} . This leaves the signal at -1.2 ppm to be due to half of the 3rd coordination sphere. These paramagnetically-displaced signals have linewidths (Γ) which range from being equivalent to the bulk signal to being 20% larger than the bulk signal. The broadening of the spectra is likely primarily due to the effect of paramagnetic Ce^{3+} on the surrounding nuclei,⁷⁴ but may also be due to non-uniform environments of the ^{27}Al nuclei around Ce^{3+} . These small Γ 's indicate a high degree of order and little distortion of the local environment of ^{27}Al nuclei near substituted Ce^{3+} . This supports the Rietveld results showing a high de-

gree of crystalline order from small ADPs, and the EXAFS results showing small MSRDs of Al atoms around Ce in YAG.

Quantification of the octahedral portion of the ^{27}Al spectra on its own offers a convincing argument for a random distribution of Ce ions that have been all reduced to Ce^{3+} in the YAG lattice, but this conclusion is further supported by examining the spin dynamics of YAG:Ce. Nuclei near substituted Ce^{3+} are expected to relax much faster than bulk nuclei due to dipolar interactions between Ce^{3+} and nearby ^{27}Al nuclei.⁶⁸ The signal from the faster-relaxing species can be isolated from that of the bulk by simply using a short recycle delay. However, a more elegant method to probe the spin dynamics of these materials is to use a saturation-recovery experiment, which is shown for $\text{Y}_{2.94}\text{Ce}_{0.06}\text{Al}_5\text{O}_{12}$ in Figure 7(b). The paramagnetically-displaced octahedral ^{27}Al signal near -15 ppm saturates in intensity much faster than the other octahedral ^{27}Al signals around 1 ppm, consistent with the conclusion that the ^{27}Al nuclei which resonate near -15 ppm are proximal to Ce^{3+} in the YAG structure. Integrated areas from fits to each spectra result in build-up curves shown in Figure 9(c), from which T_1 relaxation times can be extracted by fitting the curves of integrated intensity as a function of time with an exponential function.⁷⁵ The measured relaxation time of the signal at 3.2 ppm is the result of a mixture of 2nd- and 3rd-coordination sphere ^{27}Al nuclei, which means the relaxation time of the 2nd-coordination sphere ^{27}Al nuclei is likely much less than the value in Table 4, since the 3rd-coordination sphere ^{27}Al nuclei contributed heavily to the signal intensity of the 3.2 ppm signal. From Figure 9(c) and Table 4 it can be seen that the T_1 relaxation time decreases with increasing distance from Ce^{3+} in the YAG structure. This indicates a weaker interaction between ^{27}Al and Ce^{3+} as the ^{27}Al - Ce^{3+} distance increases, and supports the fit to the octahedral part of the ^{27}Al spectra in Figure 9(a).

A T_1 -filtered experiment can be used as another confirmation of the previous analysis, since slower-relaxing species, such as the bulk ^{27}Al signal, can be isolated from faster relaxing species by using a T_1 -filter. Such an experiment on $\text{Y}_{2.94}\text{Ce}_{0.06}\text{Al}_5\text{O}_{12}$ yields the

spectra in supporting information Figure S3, which shows an absence of intensity around the -15 ppm signal corresponding to the 1st coordination shell of ^{27}Al around Ce^{3+} . There is also missing intensity around the shoulders of the bulk signal, corresponding to the 2nd and 3rd coordination shells of octahedral ^{27}Al near Ce^{3+} . Fits to the octahedral region of the ^{27}Al NMR T_1 -filtered spectra and the difference between the single-pulse and T_1 -filtered spectra confirm the model in Figure 9(b), since in the T_1 -filtered spectra there is a lack of intensity where the 1st and 2nd shell ^{27}Al signals would otherwise be in a fully-quantitative 1D single-pulse ^{27}Al MAS NMR spectra.

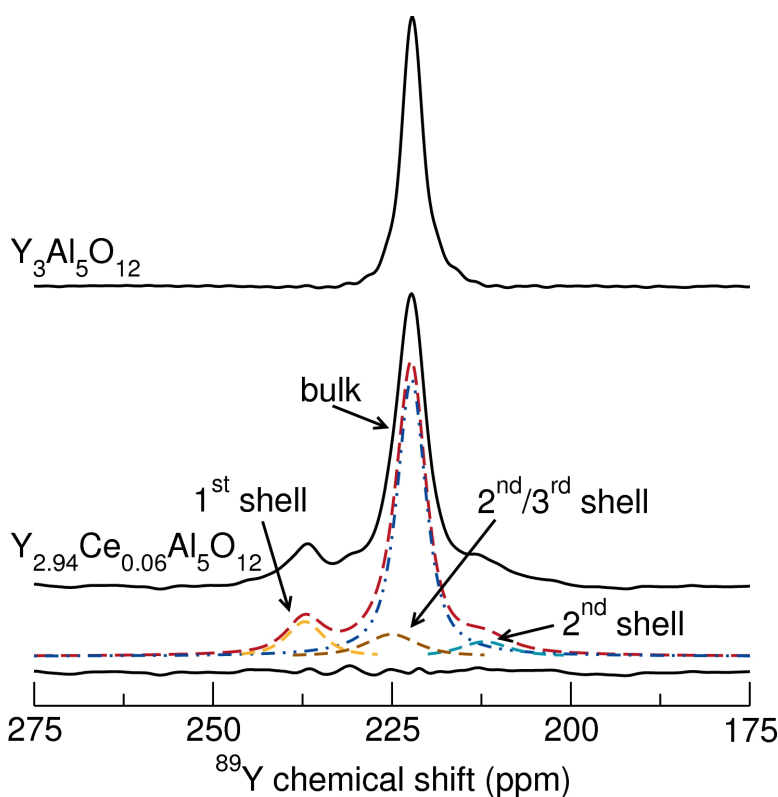


Figure 10. 1D single-pulse solid-state ^{89}Y NMR spectra (6 kHz MAS) of $\text{Y}_{3-x}\text{Ce}_x\text{Al}_5\text{O}_{12}$ with (a) $x = 0$ and (b) 0.06 taken at 295 K and 19.6 T. (b) Fit to the $x = 0.06$ Ce^{3+} -substituted material, with the difference between the fit and data shown below the spectra. The fit has been offset from the data for clarity.

The tetrahedral ^{27}Al signal from $\text{Y}_{3-x}\text{Ce}_x\text{Al}_5\text{O}_{12}$ is expected to behave analogously to the octahedral signal, but is not as simple to analyze due to the wide Pake pattern which results from a large quadrupolar moment of around 6 MHz.⁶³ However, a single peak cannot

fit the data well, as demonstrated in Figure 9(a), consistent with paramagnetic displacements of the tetrahedral ^{27}Al signal from proximal Ce^{3+} ions. The first coordination sphere of tetrahedral ^{27}Al around a substituted Ce^{3+} is assumed to be shifted in the same direction (negative ppm) as the octahedral ^{27}Al site. This signal for the first coordination sphere of tetrahedral ^{27}Al and the signal for half of the second coordination sphere were approximated as one signal, since the displacement occurs in the same direction. The other half of the second coordination sphere was predicted to move in the positive chemical shift direction and was fit accordingly. Figure 9(a) shows that the fits reproduce the data well with three peaks, however, it is possible the first coordination sphere may be shifted further toward negative ppm values. Because the tetrahedral signal is so wide, this displaced signal may broaden into the baseline. This makes concrete conclusions about the interaction of tetrahedral ^{27}Al with Ce^{3+} in YAG extremely difficult from this data. However, analysis of the relative integrated intensities for the $\text{Y}_{2.94}\text{Ce}_{0.06}\text{Al}_5\text{O}_{12}$ material shows that the first coordination shell of tetrahedral ^{27}Al accounts for about 4.3% of the total tetrahedral ^{27}Al population, which gives a Ce composition of $x = 0.0645$. This is in good agreement with the nominal amount of $x = 0.06$, and supports the model in Figure 9(a).

The paramagnetic effects of the Ce^{3+} ions in $\text{Y}_{3-x}\text{Ce}_x\text{Al}_5\text{O}_{12}$ displace the NMR signal of other nuclei as well, such as ^{89}Y , as shown in the 1D single-pulse solid-state ^{89}Y MAS NMR spectra in Figure 10. The undoped YAG material shows a single signal at 222 ppm and two spinning sidebands, which agree well with previous reports.^{64,76} Upon Ce^{3+} substitution, a separate signal appears near 237 ppm, the central signal at 222 ppm broadens, and a shoulder appears on both sides of the bulk signal at 222 ppm. These effects are again due to the paramagnetism of Ce^{3+} in YAG. Equation 1 predicts a +8 ppm displacement for two ^{89}Y nuclei and a -15 ppm displacement for the other two ^{89}Y nuclei in the first coordination sphere ($r = 3.68 \text{ \AA}$) around a substituted Ce^{3+} ion (Table 4). However, it appears the displacement occurs only in the positive direction for the first coordination sphere, indicating the interaction with Ce^{3+} is dominated by the Fermi contact shift, similar to the

effects in the ^{27}Al NMR spectra. The displacement direction is in the opposite direction of that observed for the first coordination sphere of octahedral ^{27}Al nuclei around Ce^{3+} ions. This is consistent with the fact that the Fermi contact shift is inversely proportional to the gyromagnetic ratio of the resonating nucleus, since the signs of these physical constants are opposite for ^{27}Al and ^{89}Y nuclei. The next two coordination spheres of ^{89}Y around a Ce^{3+} ion appear to interact with Ce^{3+} primarily by the through space (dipolar) mechanism. The magnitudes of the calculated displacements are less than the fitted values, which is opposite the trend found in the ^{27}Al spectra. The integrated population from the ^{89}Y spectra of $\text{Y}_{2.94}\text{Ce}_{0.06}\text{Al}_5\text{O}_{12}$ of the first coordination shell of Y around Ce^{3+} correspond to $x = 0.0825$, larger than the nominal value of 0.06. However, this is likely due to the very long T_1 relaxation time of ^{89}Y nuclei. Since the ^{89}Y nuclei near Ce^{3+} will relax faster than other ^{89}Y nuclei, the ^{89}Y nuclei near Ce^{3+} ions will have a signal larger than expected if the delay time is not sufficiently long to allow for a fully quantitative spectra, as is likely the case here.

Electron spin density sharing out to *ca.* 3.6 Å in YAG is consistent with previous observations of interactions of lanthanide-substituted inorganic materials. For example, purely dipolar interactions were observed in CaF_2 with the next-nearest neighbor at 4.53 Å, but Fermi contact was found to affect the nearest F at 2.63 Å.^{77,78} Since the YAG lattice is more covalent than CaF_2 (based on electronegativities), Fermi contacts at larger distances are not surprising. Past this first coordination sphere, the pseudocontact shift reasonably predicts the displacement directions and relative magnitudes. The sharing of electron spin density through bonds in YAG reflects the highly connected and compact nature of the structure. This connectivity leads to a rigidity that tightly holds Ce^{3+} atoms in YAG:Ce, leading to the large crystal field splitting of Ce^{3+} in YAG and the high quantum efficiency as seen from EXAFS and ADP analyses.

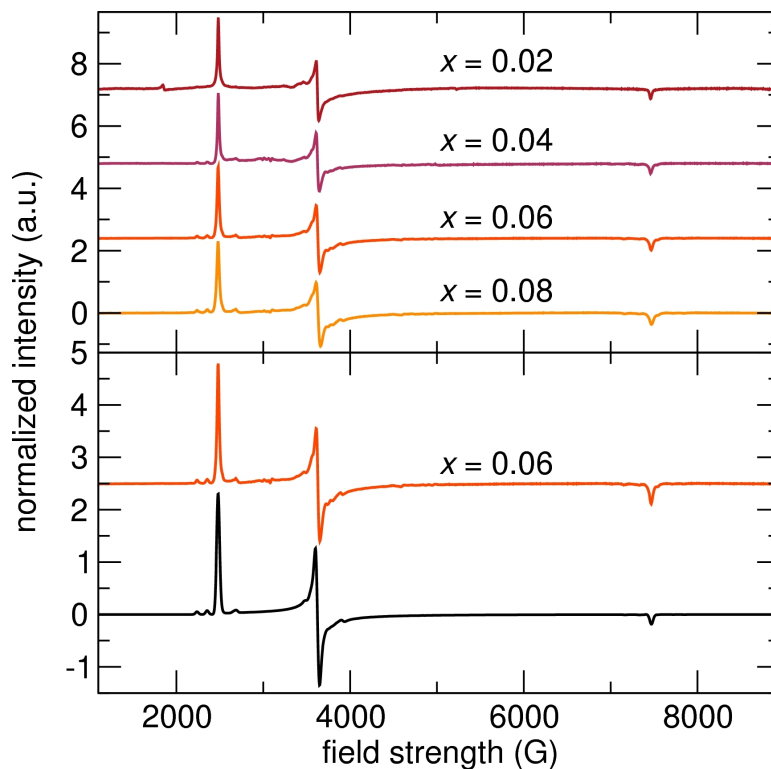


Figure 11. Powder EPR data of Ce^{3+} in $\text{Y}_{3-x}\text{Ce}_x\text{Al}_5\text{O}_{12}$ taken at 4 K and 9.4 GHz with compositions as labeled in the figure. The bottom spectrum is a simulation of the $x = 0.06$ material with 6 different Ce^{3+} sites.

Table 5. Components of the g-tensor from the powder EPR spectra of $\text{Y}_{2.94}\text{Ce}_{0.06}\text{Al}_5\text{O}_{12}$ taken at 4 K and 9.4 GHz.^a

g_x	g_y	g_z
3.03	1.94	0.946
2.88	1.90	0.924
2.73	1.86	0.908
2.69	1.81	0.899
2.55	1.79	0.878
2.52	1.73	0.864

^a The rows of g-factor components do not necessarily imply that the each row is from the same Ce site.

Evidence for Ce–Ce pairs by direct observation of the Ce³⁺ electronic environment.

While solid-state NMR spectroscopy is a sensitive tool for probing the local environment of the ²⁷Al and ⁸⁹Y nuclei in Y_{3-x}Ce_xAl₅O₁₂, EPR can be used on phosphors to investigate the local environment of the activator ions' unpaired electrons. The EPR spectra of Ce³⁺ in Y_{3-x}Ce_xAl₅O₁₂ ($x = 0.02, 0.04, 0.06, 0.08$) in Figure 11 (taken at 4K) shows the primary Ce³⁺ signals with g -tensor values of 2.73, 1.86, and 0.908 (from left to right). These values are in good agreement with values previously measured and calculated in the literature,^{79,80} and the broad range of g -tensor values indicates a large electron spin density anisotropy. Spectra from YAG:Ce materials with varying Ce concentrations show the same features. Similarly to the 1D single-pulse solid-state ²⁷Al MAS NMR spectra, the solid-state EPR spectra of YAG:Ce prepared with and without BaF₂ and NH₄F fluxes looks nearly identical, as shown in Figure S2(b). This corroborates the ²⁷Al NMR result that BaF₂ and NH₄F fluxes do not affect the local environment of Ce³⁺ in the YAG lattice. Double integration (DI) of the spectra yields a linear increase in DI value with Ce content (supporting information Figure S4(b)), suggesting all Ce is incorporated into the YAG lattice and is reduced to Ce³⁺ during the reaction, corroborating the XANES, synchrotron X-ray, and ²⁷Al NMR results. The Γ of the main signal in the EPR spectra at $B_o = 2480$ G varies linearly with Ce concentration (supporting information Figure S4(a)), which indicates the presence of Ce–Ce dipolar couplings.⁸¹ Small satellite signals reside near the main Ce³⁺ signals, which have been previously attributed to Ce³⁺ in slightly disturbed (distinct) lattice sites in both YAG⁷⁹ and YAlO₃⁸² EPR spectra. There appear to be six distinct Ce sites in the YAG:Ce lattice, manifesting six sets of distinct g -tensor values shown in Table 5. The small satellite signals are present near all three major features in the spectra, shown in supporting information Figure S5. A simulation using the parameters in Table 5 shown at the bottom of Figure 11 shows that the data can be simulated well with six distinct Ce sites.

To confirm that the satellite signals were from Ce³⁺ and not another unpaired electron, temperature-dependent EPR spectra were taken for the Y_{2.94}Ce_{0.06}Al₅O₁₂. Since the

satellite signals remained and broadened at the same rate as the main YAG:Ce signals with increasing temperature, the satellite signals were confirmed to come from Ce^{3+} in YAG. The linewidths of the peaks were found to follow the Orbach law, and the γ of the signal at 2480 G was fitted using the equation $\Gamma = (e^{\Delta/k_B T} - 1)^{-1} + C$.^{83,84} From the fit shown in supporting information Figure S4(c), a value of 14 cm^{-1} was obtained, which is the splitting between the lowest two ${}^2F_{5/2}$ levels of Ce^{3+} .

A previous EPR study attributed the satellite peaks to Ce in disturbed lattice sites, but was unspecific as to what the perturbation was.⁷⁹ A separate study correlating the concentration of Ce in YAG to the optical properties suggested that some lower-energy Ce^{3+} sites are present, which may be due to perturbed lattice sites or Ce–Ce pairs in the structure.¹⁶ For the $x = 0.06$ material measured here, a random distribution of Ce in the lattice would result in about 8% of Ce–Ce pairs. From a fit to the g_x region (shown in supporting information Figure S5), the population of Ce in sites other than the main Ce site is around 8.8 % of Ce ions. This agrees quite well with the population of Ce–Ce pairs expected for a random distribution of Ce in the YAG lattice, suggesting that the satellite peaks result from two Ce atoms in neighboring Y sites. This result corroborates the RMC and ${}^{27}\text{Al}$ NMR results, which are consistent with a random distribution of Ce in the YAG lattice.

CONCLUSIONS

A combined spectroscopic and scattering study has revealed detailed insights about the local structure of the Ce^{3+} ion in $\text{Y}_{3-x}\text{Ce}_x\text{Al}_5\text{O}_{12}$. Synchrotron X-ray scattering showed that the YAG unit cell expands slightly with increasing amounts of Ce (about a 0.03% increase from $x = 0$ to $x = 0.06$). Ce K-edge XANES and ${}^{27}\text{Al}$ NMR results show that all the Ce in the YAG lattice is reduced to Ce^{3+} , and that the lattice near substituted Ce is well ordered and rigid. Ce K-edge EXAFS reveals a 3% expansion in Ce–O bond distance compared to

the Y-O average structure distance, and small MSRDS near Ce, which is related to the high quantum efficiency in YAG:Ce. The distortion of the YAG lattice around substituted Ce decreases with increasing distance from Ce, and is measurable up to the 5th coordination shell (3.7 Å) from EXAFS. RMC simulations, ^{27}Al NMR spectra, and EPR results are all consistent with a random distribution of Ce in the YAG lattice. Analysis of ADPs and calculation of θ_D shows YAG is a very rigid lattice, with many inaccessible phonon modes available at LED operating temperatures. The observed decrease in θ_D with increasing Ce substitution is related to the quenching of luminescence with increasing Ce substitution, since more phonon modes are available at a given temperature for YAG materials with a higher Ce content. ^{27}Al and ^{89}Y NMR experiments also show that the unpaired $4f$ electron in Ce^{3+} causes a displacement in the NMR signal of nearby nuclei, as well as a greatly shortened T_1 relaxation time of nearby nuclei. Integration of ^{27}Al NMR results with Ce composition show the nominal amount of Ce is indeed incorporated into the lattice as Ce^{3+} . EPR spectra of the YAG:Ce phosphor show small satellite signals around the main absorption signal, suggesting Ce–Ce pairs are present in the amount expected from a random distribution of Ce in the YAG structure.

Acknowledgement

The authors would like to thank Ryan Davis for assistance with EXAFS fitting and Alexander Mikhailovsky for assistance with quantum efficiency measurements. N.C.G. has been supported by the ConvEne IGERT Program (NSF-DGE 0801627). The research carried out here made extensive use of shared experimental facilities of the Materials Research Laboratory: The MRL Central Facilities are supported by the MRSEC Program of the NSF under Award No. DMR 1121053; a member of the NSF-funded Materials Research Facilities Network (www.mrfn.org). Use of the Advanced Photon Source at Argonne National Laboratory was supported by the U. S. Department of Energy, Office of Science, Office of Basic Energy Sciences, under Contract No. DE-AC02-06CH11357. The authors thank Joan

Siewenie for assistance with data collection at NPDF. This work has benefited from the use of NPDF and HIPD at the Lujan Center, funded by DOE Office of Basic Energy Sciences; LANL is operated by Los Alamos National Security LLC under DE-AC52-06NA25396. RMC simulations were performed on the Hewlett Packard QSR cluster at the CNSI-MRL High Performance Computing Facility. We acknowledge support from the Center for Scientific Computing at the CNSI and MRL: an NSF MRSEC (DMR-1121053) and NSF CNS-0960316.

References

- (1) Shur, M. S.; Zukauskas, R. P. *IEEE* **2005**, *93*, 1691–1703.
- (2) Krames, M. R.; Shchekin, O. B.; Mueller-Mach, R.; Mueller, G. O.; Zhou, L.; Harbers, G.; Craford, M. G. *J. Disp. Technol.* **2007**, *3*, 160–175.
- (3) Nakamura, S.; Fasol, G.; Pearton, S. J. *The Blue Laser Diode: The Complete Story*, 2nd ed.; Springer, 2000.
- (4) Shimizu, Y.; Sakano, K.; Noguchi, Y.; Moriguchi, T. Light emitting device having a nitride compound semiconductor and a phosphor containing a garnet fluorescent material. 1999; U.S. Patent 5,998,925.
- (5) Reeh, U.; Höhn, K.; Stath, N.; Waitl, G.; Schlotter, P.; Schneider, J.; Schmidt, R. Light-radiating semiconductor component with a luminescence conversion element. 2004; U.S. Patent 6,812,500B2.
- (6) Doxsee, D. D.; Setlur, A. A.; Brown, Z. R.; Srivastava, A.; Comanzo, H. White light LED device. 2005; U.S. Patent 6,963,857B2.
- (7) Blasse, G.; Bril, A. *Appl. Phys. Lett* **1967**, *11*.
- (8) Nakamura, S.; Mukai, T.; Senoh, M. *Appl. Phys. Lett.* **1994**, *64*, 1687–1689.

- (9) Yen, W. M.; Shionoya, S.; Yamamoto, H. *Phosphor Handbook*, 2nd ed.; Taylor & Francis Group, 2007.
- (10) Blasse, G. *J. Chem. Phys.* **1967**, *47*, 5139.
- (11) Ronda, C. R. *Luminescence: From Theory to Applications*; John Wiley & Sons, 2004.
- (12) Bachmann, V.; Ronda, C.; Meijerink, A. *Chem. Mater.* **2009**, *21*, 2077–2084.
- (13) Robbins, D. J. *J. Electrochem. Soc.* **1979**, *126*, 1550–1555.
- (14) Tien, T. Y.; Gibbons, E. F.; DeLosh, R. G.; Zacmanidis, P. J.; Smith, D. E.; Stadler, H. L. *J. Electrochem. Soc.* **1973**, *120*, 278–281.
- (15) Robbins, D. J.; Cockayne, B.; Lent, B.; Glasper, J. L. *J. Electrochem. Soc.* **1979**, *126*, 1556–1563.
- (16) Setlur, A.; Srivastava, A. *Opt. Mater.* **2007**, *29*, 1647–1652.
- (17) Wu, J. L.; Gundiah, G.; Cheetham, A. *Chem. Phys. Lett.* **2007**, *441*, 250–254.
- (18) Furman, J.; Gundiah, G.; Page, K.; Pizarro, N.; Cheetham, A. *Chem. Phys. Lett.* **2008**, *465*, 67–72.
- (19) Pan, Y.; Wang, W.; Liu, G.; Skanthakumar, S.; Rosenberg, R.; Guo, X.; Li, K. K. *J. Alloys Compd.* **2009**, *488*, 638–642.
- (20) Gracia, J.; Seijo, L.; Barandiarán, Z.; Curulla, D.; Niemansverdriet, H.; van Genip, W. *J. Lumin.* **2008**, *128*, 1248–1254.
- (21) Muñoz-García, A. B.; Seijo, L. *J. Phys. Chem. A* **2011**, *115*, 815–823.
- (22) Ghigna, P.; Pin, S.; Ronda, C.; Speghini, A.; Piccinelli, F.; Bettinelli, M. *Opt. Mater.* **2011**, *34*, 19–22.

- (23) Wang, J.; Toby, B. H.; Lee, P. L.; Ribaud, L.; Antao, S. M.; Kurtz, C.; Ramanathan, M.; Von Dreele, R. B.; Beno, M. A. *Rev. Sci. Instrum.* **2008**, *79*, 085105–085105–7.
- (24) Proffen, T.; Billinge, S. J. L.; Egami, T.; Louca, D. Z. *Kristallogr.* **2003**, *218*, 132–143.
- (25) Tucker, M. G.; Dove, M. T.; Keen, D. A. *J. Appl. Crystallogr.* **2001**, *34*, 630–638.
- (26) Shoemaker, D. P.; Li, J.; Seshadri, R. *J. Am. Chem. Soc.* **2009**, *131*, 11450–11457.
- (27) Tucker, M. G.; Keen, D. A.; Evans, J. S. O.; Dove, M. T. *J. Phys.-Condens. Mat.* **2007**, *19*, 335215.
- (28) Yü, Q. M. *Mater. Sci. Forum* **2010**, 663-665, 177–182.
- (29) Xu, S.; Sun, L.; Zhang, Y.; Ju, H.; Zhao, S.; Deng, D.; Wang, H.; Wang, B. *J. Rare Earth.* **2009**, *27*, 327–329.
- (30) Bérar, J. F.; Garnier, P. *NIST Special Publ.* **1992**, *846*, 212.
- (31) Toby, B. H. *J. Appl. Crystallogr.* **2001**, *34*, 210–213.
- (32) Momma, K.; Izumi, F. *J. Appl. Crystallogr.* **2011**, *44*, 1272–1276.
- (33) Peterson, P. F.; Gutmann, M.; Proffen, T.; Billinge, S. J. L. *J. Appl. Crystallogr.* **2000**, *33*, 1192–1192.
- (34) Egami, T.; Billinge, S. J. L. *Underneath the Bragg Peaks: Structural Analysis of Complex Materials*; Elsevier: Kidlington, Oxford, UK, 2003.
- (35) Farrow, C. L.; Juhas, P.; Liu, J. W.; Bryndin, D.; BoÅćin, E. S.; Bloch, J.; Proffen, T.; Billinge, S. J. L. *J. Phys.-Condens. Mat.* **2007**, *19*, 335219.
- (36) McGreevy, R. L. *J. Phys.-Condens. Mat.* **2001**, *13*, R877.
- (37) Tucker, M. G.; Keen, D. A.; Dove, M. T.; Goodwin, A. L.; Hui, Q. *J. Phys.-Condens. Mat.* **2007**, *19*, 335218.

- (38) Heald, S.; Stern, E.; Brewster, D.; Gordon, R.; Crozier, D.; Jiang, D.; Cross, J. J. *Synchrotron Radiat.* **2001**, *8*, 342–344.
- (39) Skanthakumar, S.; Soderholm, L. *Phys. Rev. B* **1996**, *53*, 920–926.
- (40) Newville, M. *J. Synchrotron Radiat.* **2001**, *8*, 322–324.
- (41) Fenzke, D.; Freude, D.; Fröhlich, T.; Haase, J. *Chem. Phys. Lett.* **1984**, *111*, 171–175.
- (42) Woessner, D.; Timken, H. *J. Magn. Reson.* **1990**, *90*, 411–419.
- (43) Yesinowski, J. P. *J. Magn. Reson.* **2006**, *180*, 147–161.
- (44) Massiot, D.; Fayon, F.; Capron, M.; King, I.; Le Calvé, S.; Alonso, B.; Durand, O., Jean; Bujoli, B.; Gan, Z.; Hoatson, G. *Magn. Reson. Chem.* **2002**, *40*, 70–76.
- (45) Stoll, S.; Schweiger, A. *J. Magn. Reson.* **2006**, *178*, 42–55.
- (46) Robbins, D. J.; Cockayne, B.; Lent, B.; Duckworth, C. N.; Glasper, J. L. *Phys. Rev. B* **1979**, *19*, 1254–1269.
- (47) Brese, N. E.; O’Keeffe, M. *Acta Crystallogr. B* **1991**, *47*, 192–197.
- (48) Wynne, R.; Daneu, J. L.; Fan, T. Y. *Appl. Optics* **1999**, *38*, 3282–3284.
- (49) Mellergård, A.; McGreevy, R. L. *Acta Crystallogr. A* **1999**, *55*, 783–789.
- (50) McGreevy, R. L. *Nucl. Instrum. Meth. A* **1995**, *354*, 1 – 16.
- (51) Trzesowska, A.; Kruszynski, R.; Bartczak, T. J. *Acta Crystallogr. B* **2004**, *60*, 174–178.
- (52) Shannon, R. D. *Acta Crystallogr. A* **1976**, *32*, 751–767.
- (53) Özen, G.; Demirata, B. *Spectrochim. Acta A*: **2000**, *56*, 1795–1800.
- (54) Willis, B. T. M.; Pryor, A. W. *Thermal vibrations in crystallography*; Cambridge University Press, 1975.

- (55) Cowley, J. M. *Diffraction Physics*; North-Holland Physics Publishing, 1981.
- (56) Diehl, R.; Brandt, G. *Mater. Res. Bull.* **1975**, *10*, 85–90.
- (57) Redfern, S. A. T.; Harrison, R. J.; O'Neill, H. S. C.; Wood, D. R. R. *Am. Mineral.* **1999**, *84*, 299–310.
- (58) Vasylechko, L.; Senyshyn, A.; Trots, D.; Niewa, R.; Schnelle, W.; Knapp, M. *J. Solid State Chem.* **2007**, *180*, 1277–1290.
- (59) Aggarwal, R. L.; Ripin, D. J.; Ochoa, J. R.; Fan, T. Y. *J. Appl. Phys.* **2005**, *98*, 103514–103514–14.
- (60) Pujol, M. C.; Solé, R.; Massons, J.; Gavaldà, J.; Solans, X.; Zaldo, C.; Díaz, F.; Aguiló, M. *J. Appl. Crystallogr.* **2001**, *34*, 1–6.
- (61) Sales, B.; Chakoumakos, B.; Mandrus, D.; Sharp, J. J. *J. Solid State Chem.* **1999**, *146*, 528–532.
- (62) Pauling, L. *J. Am. Chem. Soc.* **1929**, *51*, 1010–1026.
- (63) Massiot, D.; Bessada, C.; Coutures, J. P.; Taulelle, F. *J. Mag. Res.* **1990**, *90*, 231–242.
- (64) Florian, P.; Gervais, M.; Douy, A.; Massiot, D.; Coutures, J.-P. *J. Phys. Chem. B* **2001**, *105*, 379–391.
- (65) Lin, Y. S.; Tseng, Y. H.; Liu, R. S.; Chan, J. C. C. *J. Electrochem. Soc.* **2007**, *154*, P16–P19.
- (66) Harazono, T.; Yokota, E.; Uchida, H.; Watanabe, T. *B. Chem. Soc. Jpn.* **1998**, *71*, 2797–2805.
- (67) Grey, C. P.; Dobson, C. M.; Cheetham, A. K.; Jakeman, R. J. B. *J. Am. Chem. Soc.* **1989**, *111*, 505–511.

- (68) Grey, C. P.; Smith, M. E.; Cheetham, A. K.; Dobson, C. M.; Dupree, R. *J. Am. Chem. Soc.* **1990**, *112*, 4670–4675.
- (69) Kuklja, M. M. *J. Phys.-Condens. Mat.* **2000**, *12*, 2953–2967.
- (70) Bleaney, B. *J. Mag. Res.* **1972**, *8*, 91–100.
- (71) Carrington, A.; McLachlan, A. D. *Introduction to Magnetic Resonance*; Harper and Row: New York, 1967.
- (72) Morrison, C. A.; Wortman, D. E.; Karayianis, N. *J. Phys. C: Solid State Phys.* **1976**, *9*, L191–L194.
- (73) Freeman, A. J.; Watson, R. E. *Phys. Rev.* **1962**, *127*, 2058–2075.
- (74) Van Vleck, J. H. *Phys. Rev.* **1948**, *74*, 1168–1183.
- (75) Levitt, M. H. *Spin Dynamics: Basics of Nuclear Magnetic Resonance*, 2nd ed.; Wiley, 2008.
- (76) Harazono, T.; Watanabe, T. B. *Chem. Soc. Jpn.* **1997**, *70*, 2383–2388.
- (77) Bessent, R. G.; Hayes, W. *Proceedings of the Royal Society of London. Series A. Mathematical and Physical Sciences* **1965**, *285*, 430–444.
- (78) Baker, J. M.; Hurrell, J. P. *Proceedings of the Physical Society* **1963**, *82*, 742–756.
- (79) Baur, J.; Schlotter, P.; Schneider, J. *Adv. Solid State Phys.* **1998**, *37*, 67–78.
- (80) Lewis, H. R. *J. Appl. Phys.* **1966**, *37*, 739.
- (81) Abragam, A.; Bleaney, B. *Electron paramagnetic resonance of transition ions*; Clarendon P., 1970.
- (82) Asatryan, H.; Rosa, J.; Mareš, J. *Solid State Commun.* **1997**, *104*, 5–9.

(83) Orbach, R. *P. Roy. Soc. Lond. A. Mat.* **1961**, *264*, 458–484.

(84) Yen, W. M.; Scott, W. C.; Scott, P. L. *Phys. Rev.* **1965**, *137*, A1109–A1112.